Rigidized 3-aminocoumarins as fluorescent probes for strongly acidic environments and rapid yeast vacuolar lumen staining: Mechanism and application

Jakub Joniak, [a] Henrieta Stankovičová, [a] Šimon Budzák, [b] Milan Sýkora, [c] Katarína Gaplovská-Kyselá, [d] Juraj Filo [a] and Marek Cigáň *[a]

[a] *Department of Organic Chemistry, Faculty of Natural Sciences, Comenius University, 842 15 Bratislava, Slovakia*

[b] *Department of Chemistry, Faculty of Natural Sciences, Matej Bel University, 974 01 Banská Bystrica, Slovakia*

[c] *Laboratory for Advanced Materials, Faculty of Natural Sciences, Comenius University, 842 15 Bratislava, Slovakia*

[d] *Department of Genetics, Faculty of Natural Sciences, Comenius University, 842 15 Bratislava, Slovakia*

* - corresponding author

Coumarins remain one of the most important group of fluorescent bio-probes, thanks to their high quantum yields, moderate photostability, efficient cell permeation and low (cyto)toxicity. Herein, we introduce new 3-aminocoumarins as turn-on pH probes for strongly acidic conditions and indicators capable of significantly improved yeast vacuolar lumen staining compared to the commercial CMAC derivatives. We present the details of the on-off switching mechanism revealed by the TD-DFT and *ab initio* calculations complemented by a Franck-Condon analysis of the probes´ emission profiles.

Supporting Information (SI)

Table of contents

1. Synthesis

## 1.2 General Experimental Information

All reactions were carried out using oven-dried glassware and magnetic stirring. Reaction temperatures are reported as the temperature of the bath surrounding the vessel. Analytical thin layer chromatography was performed on silica gel aluminium plates or aluminium oxide neutral aluminium plates with F-254 indicator and visualized by UV light (254 nm, 360 nm). Column chromatography/flash chromatography was performed using 0.040-0.063 mm (230-400 mesh ASTM) silica gel or 0.063-0.200 mm (70-230 mesh ASTM) aluminium oxide active neutral (activity stage III). Melting points were measured on a BÜCHI M-565 melting point apparatus (BÜCHI Labortechnik AG, Flawil, Switzerland) in open capillaries. The ^{1}H and ^{13}C NMR spectra were recorded at 600 MHz and at 151 MHz, respectively, in a 5-mm NMR tube on a Varian VNMRS 600 MHz spectrometer (Agilent, Santa Clara, CA, USA) in CDCl$_3$ or DMSO-d_6 with tetramethylsilane as internal standard. Chemical shift values were recorded in δ units (ppm) and coupling constants (J) are reported in Hertz (Hz). The following abbreviations are used: s = singlet, d = doublet, dd = doublet of doublets, m = multiplet, t = triplet, bs = broad singlet. IR spectra were acquired on a Cary 630 FTIR spectrometer (Agilent, Santa Clara, CA, USA) and $\tilde{v}$ of recorded IR-signals (ATR) are given in wavenumbers (cm^{-1}). HRMS spectra were recorded on an Orbitrap Velos Pro spectrometer (Thermo Scientific, Waltham, MA, USA) in positive mode (mass range m/z 80-600, full scan, capillary temperature 350°C, heater temperature 300°C, resolution 120 000) and exact masses are given for previously unreported compounds.

1.3. Materials

Solvents not required to be dry were purchased as analytical grade and used as received. Dry solvents were freshly collected from a dry solvent purification system prior to use. Unless otherwise indicated, reagents and substrates were purchased from commercial sources (Acros Organics, Geel, Belgium; Sigma Aldrich, St. Louis, MO, USA) and used as received. All reported compounds were characterized by ^{1}H, ^{13}C NMR and IR spectra and compared with literature data. All new compounds were fully characterized by melting point, ^{1}H, ^{13}C NMR, IR and HRMS techniques.

1.4. Synthesis of Compounds

The target compounds **1-3** can be readily synthesised, as shown in Scheme S1. The first step of the synthesis is the reaction of 8-hydroxyjulolidine-9-carboxaldehyde with ethyl nitroacetate under Knoevenagel type condensation conditions followed by reduction resulting in amino derivative **1.** This compound appeared to be a suitable substrate for monoalkylation leading to monomethyl derivative **2** and reductive amination reaction with paraformaldehyde resulting in dimethylamino derivative **3**. As an alternative to the amination reaction, thermal demethylation of quarternary ammonium salt was used to synthesize the dimethylamino derivative **3** too.
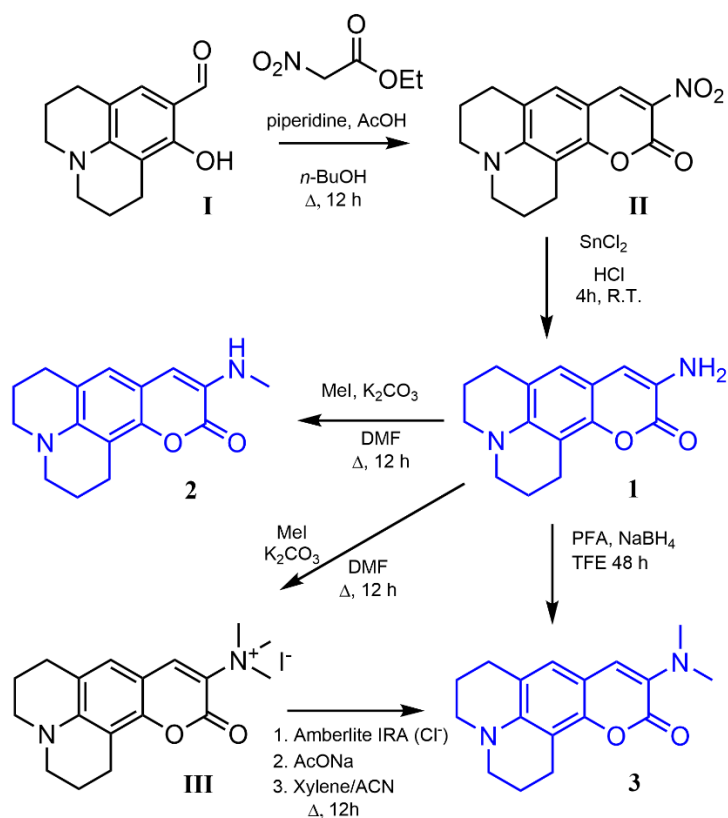
Scheme S1

Synthesis of 10-amino-2,3,6,7-tetrahydro-1*H*,5*H*-quinolizino[9,1-*gh*]coumarin (**1**)

Step 1
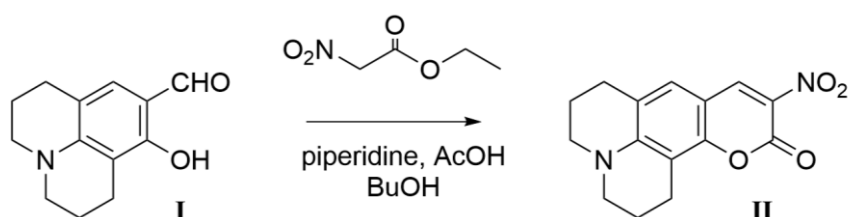
A solution of 8-hydroxyjulolidine-9-carboxaldehyde (**I**) (0.696 g, 3.2 mmol, 1 equiv.), ethyl nitroacetate (0.43 mL, 0.51 g, 3.84 mmol, 1.2 equiv.), piperidine (0.1 mL) and glacial acetic acid (0.2 mL) in dry *n*-butanol (10 mL), under argon atmosphere, was refluxed overnight. Then the reaction mixture was cooled to room temperature, precipitate formed was filtered off, washed with *n*-butanol (20 mL) and hexanes (30 mL). 10-Nitro-2,3,6,7-tetrahydro-1*H*,5*H*-quinolizino[9,1-*gh*]coumarin (**II**) was collected as purple crystalline solid (0.708 g, 77% yield) which was used for the next synthesis.

mp: 248-249 °C (*n*-BuOH).
¹H NMR (600 MHz, DMSO-*d₆*): δ 8.82 (s, 1H), 7.30 (s, 1H), 3.41 (dd, *J* = 11.4, 5.4 Hz, 4H), 2.70 (t, *J* = 5.4 Hz, 4H), 1.91–1.86 (m, 4H). ¹H NMR data are in accordance with the literature.[1]
¹³C NMR (151 MHz, CDCl₃): δ 153.8, 153.7, 150.7, 142.9, 128.2, 125.4, 121.1, 106.3, 106.0, 50.7, 50.2, 27.3, 20.8, 19.9, 19.8.
¹³C NMR (151 MHz, DMSO-*d₆*): δ 153.5, 151.1, 143.7, 129.2, 124.6, 121.4, 106.5, 105.4, 50.5, 50.0, 27.1, 20.7, 19.8, 19.7.
IR (neat, cm⁻¹): ṽ 2941, 2855, 1723, 1623, 1520, 1362, 1260, 1180.

Step 2
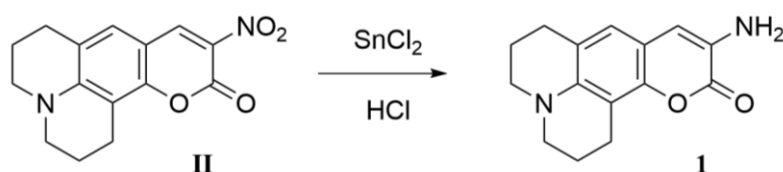
SnCl₂ (1.75 g, 9.23 mmol, 4.1 equiv.) was added to a fuming HCl (10 mL) and the mixture was stirred at room temperature for 5 min. After dissolving of SnCl₂, nitrocoumarin **II** (0.63 g, 2.20 mmol, 1 equiv.) was slowly added in three portions and the reaction mixture was stirred at room temperature for 4 h. Then the mixture was poured over ice (100 mL), neutralized with 5M aq. NaOH, stirred at room temperature for 1 h and extracted with Et₂O (3x50 mL). The combined organic layers were dried over MgSO₄ and concentrated in vacuo to yield coumarin **1** as orange crystalline solid (0.532 g, 94% yield).

mp: 126-126.5 °C (Et₂O); **mp**[1]:123-124 °C.
¹H NMR (600 MHz, DMSO-*d₆*) δ 6.78 (s, 1H), 6.61 (s, 1H), 4.96 (s, 2H), 3.12 (dd, *J* = 10.8, 5.4 Hz, 4H), 2.72 (t, *J* = 6.6 Hz, 2H), 2.69 (t, *J* = 6.6 Hz, 2H), 1.93–1.83 (m, 4H). ¹H NMR data are in accordance with the literature.[1]
¹³C NMR (151 MHz, DMSO-*d₆*) δ 159.8, 146.1, 142.1, 128.9, 122.5, 118.9, 112.1, 110.5, 106.9, 49.7, 49.3, 27.3, 21.9, 21.1, 20.6.
IR (neat, cm⁻¹): ṽ 3406, 3323, 2929, 2834, 1681, 1610, 1559, 1301, 1150.
HRMS-ESI: Calc. for C₁₅H₁₇N₂O₂ [M+H]⁺ 257.1290, found 257.1282.

Synthesis of 10-methylamino-2,3,6,7-tetrahydro-1*H*,5*H*-quinolizino[9,1-*gh*]coumarin (**2**)
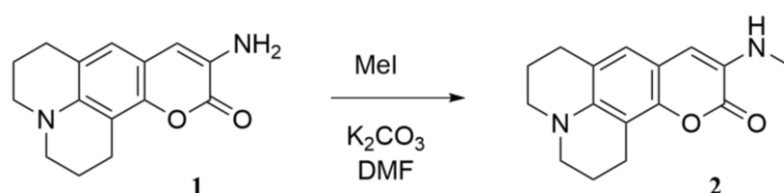
K₂CO₃ (92 mg, 0.668 mmol, 4 equiv.) and MeI (21 μL, 48 mg, 0.34 mmol, 2 equiv.) were added to a solution of aminocoumarin **1** (43 mg, 0.167 mmol, 1 equiv.) in DMF (0.5 mL) and the reaction mixture was stirred at 50°C overnight. Volatiles were evaporated under reduced pressure, the residue was redissolved in H₂O (2 mL) and extracted with DCM (3x2 mL). Combined organic layers were dried over MgSO₄, evaporated and the crude was purified by column chromatography (silica gel, hexanes/DCM 100:0 to 4:3) followed by another column chromatography (Al₂O₃, hexanes/EtOAc 100:0 to 99.5:0.5) to give product **2** as orange crystalline solid (19 mg, 42% yield).

mp: 141-142 °C.
¹H NMR (600 MHz, CDCl₃): δ 6.77 (s, 1H), 6.25 (s, 1H), 4.46 (s, 1H), 3.17-3.14 (m, 4H), 2.89 (t, J = 6.6 Hz, 2H), 2.83 (s, 3H), 2.77 (t, J = 6.6 Hz, 2H), 2.01- 1.95 (m, 4H).
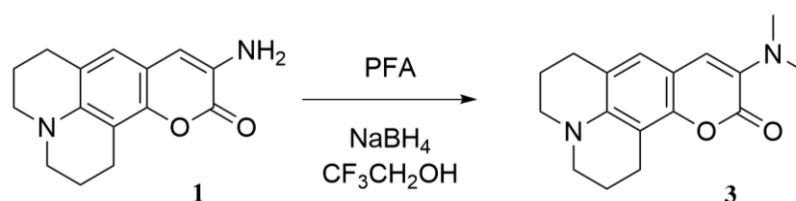**¹³C NMR** (151 MHz, CDCl₃): δ 160.5, 149.7, 145.3, 141.8, 130.6, 122.4, 118.8, 110.9, 107.7, 50.2, 49.7, 30.2, 27.5, 21.9, 21.0, 20.4.
IR (neat, cm⁻¹): ṽ 3390, 2841, 1669, 1610, 1491, 1293, 1167.
HRMS-ESI: Calc. for C₁₆H₁₉N₂O₂ [M+H]⁺ 271.1447, found 271.1434.


Synthesis of 10-dimethylamino-2,3,6,7-tetrahydro-1*H*,5*H*-quinolizino[9,1-*gh*]coumarin (**3**)

Method A

Following a modified literature procedure.[2] NaBH₄ (60 mg, 1.58 mmol, 4 equiv.) was added to a mixture of aminocoumarin **1** (100 mg, 0.39 mmol, 1 equiv.) and paraformaldehyde (110 mg, 3.66 mmol, 9.4 equiv.) in trifluoroethanol (5 mL), and the reaction mixture was refluxed for 24 h. More NaBH₄ (30 mg, 0.79 mmol, 2 equiv.) was added and the mixture was refluxed for another 24 h. After the reaction was completed, the mixture was cooled to room temperature, filtered and solids were washed with trifluoroethanol (2 mL). Filtrate was concentrated in vacuo and the crude product was purified by chromatography (combiflash, 24 g silica gel, hexanes/EtOAc 95:5, 20 mL/min) and by preparative TLC (hexanes/EtOAc, 3:1). The product **3** was collected as brown-yellow oil (18 mg, 16% yield) which solidifies upon standing.

Method B
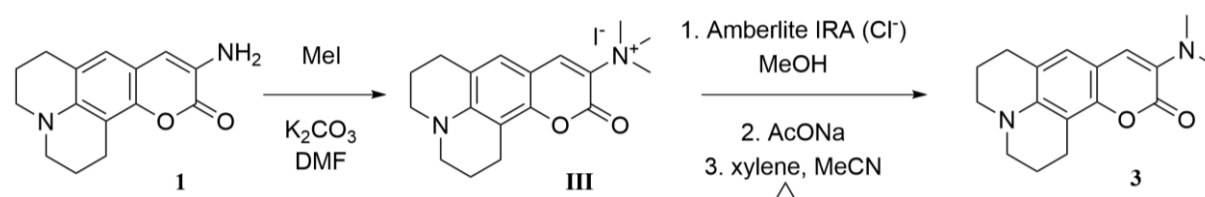
K$_2$CO$_3$ (0.431 g, 3.12 mmol, 8 equiv) was added to a solution of aminocoumarin **1** (100 mg, 0.39 mmol, 1 equiv.) in DMF (1 mL) followed by dropwise addition of MeI (98 μL, 0.223 g, 1.57 mmol, 4 equiv.), and the reaction mixture was stirred at 50°C overnight. After the reaction was completed, solvent was evaporated, the residue was redissolved in H$_2$O (4 mL) and extracted with DCM (3x4 mL). Combined organic layers were dried over MgSO$_4$, solvent was removed in vacuo and crude was triturated with Et$_2$O. 10-Trimethylammonium-2,3,6,7-tetrahydro-1*H*,5*H*-quinolizino[9,1-*gh*]coumarin iodide **III** was collected as orange crystalline compound (122 mg, 74% yield) and was used in the next step without further purification.

Following a modified literature procedure.[3] A column of Amberlite I.R.A. 400 (chloride form) was washed with aqueous solution of NaOAc (20 %) until the eluate was free from Cl$^-$. The resin was then washed with H$_2$O and finally with MeOH, until eluates, in each case, left no residue on evaporation. Solution of trimethylammonium iodide derivative **III** (122 mg, 0.29 mmol) in MeOH was then passed through the column. Solvent was removed in vacuo to afford trimethylammonium acetate of derivative **III** (90 mg, 88% yield) as highly hygroscopic orange crystalline compound. Trimethylammonium acetate salt of **III** was dissolved in dry xylene (8 mL) and dry ACN (8 mL) and the solution was refluxed under argon atmosphere overnight. Volatiles were removed under reduced pressure and the residue was partitioned between H$_2$O and EtOAc. The organic layer was dried over MgSO$_4$, concentrated and the crude was purified by column chromatography (Al$_2$O$_3$, hexanes/EtOAc, 100:0 to 99.5:0.5). The product **3** was collected as brown-yellow oil (26 mg, 57% yield; 31% yield overall) which solidified upon standing.

mp: 84-86 °C.
¹H NMR (600 MHz, CDCl$_3$): δ 6.78 (s, 1H), 6.71 (s, 1H), 3.21-3.18 (m, 4H), 2.89 (t, *J* = 6.6 Hz, 2H), 2.81 (s, 6H), 2.76 (t, *J* = 6.6 Hz, 2H), 2.00-1.94 (m, 4H).
¹³C NMR (151 MHz, CDCl$_3$): δ 160.1, 147.9, 143.3, 133.8, 123.3, 122.1, 118.6, 109.3, 106.9, 50.0, 49.6, 42.1, 27.5, 21.8, 20.9, 20.5.
IR (neat, cm^{-1}): ṽ 2821, 1687, 1610, 1307, 1073.
HRMS-ESI: Calc. for C$_{17}$H$_{21}$N$_2$O$_2$ [M+H]$^+$ 285.1603, found 285.1594.

10-Trimethylammonium-2,3,6,7-tetrahydro-1*H*,5*H*-quinolizino[9,1-*gh*]coumarin iodide **(III)** (crude)
mp: 145-146.5 °C (crude).
¹H NMR (600 MHz, DMSO-*d$_6$*): δ 8.40 (s, 1H), 7.20 (s, 1H), 3.59 (s, 9H), 3.31 (unrecognizable), 2.74 (t, 4H), 1.90-1.87 (m, 4H), 1.09 (t, 2H).
¹H NMR (600 MHz, CDCl$_3$): δ 8.87 (s, 1H), 7.41 (s, 1H), 3.95 (s, 9H), 3.34 (bs, 4H), 2.84 (t, *J* = 6.6 Hz, 2H), 2.78 (t, *J* = 6 Hz, 2H), 1.99-1.93 (m, 4H).
¹³C NMR (151 MHz, CDCl$_3$): δ 156.3, 151.6, 148.7, 138.5, 128.1, 120.9, 120.7, 105.5, 105.3, 56.2, 50.3, 49.8, 27.4, 20.9, 20.0, 19.9.
¹³C NMR (151 MHz, DMSO-*d$_6$*): δ 156.1, 151.1, 148.0, 138.2, 127.2, 122.8, 120.3, 105.3, 105.1, 54.9, 49.9, 49.3, 27.3, 21.0, 20.0.
IR (neat, cm^{-1}): ṽ 2942, 1697, 1621, 1297, 1178.

1.5. MS Spectroscopy
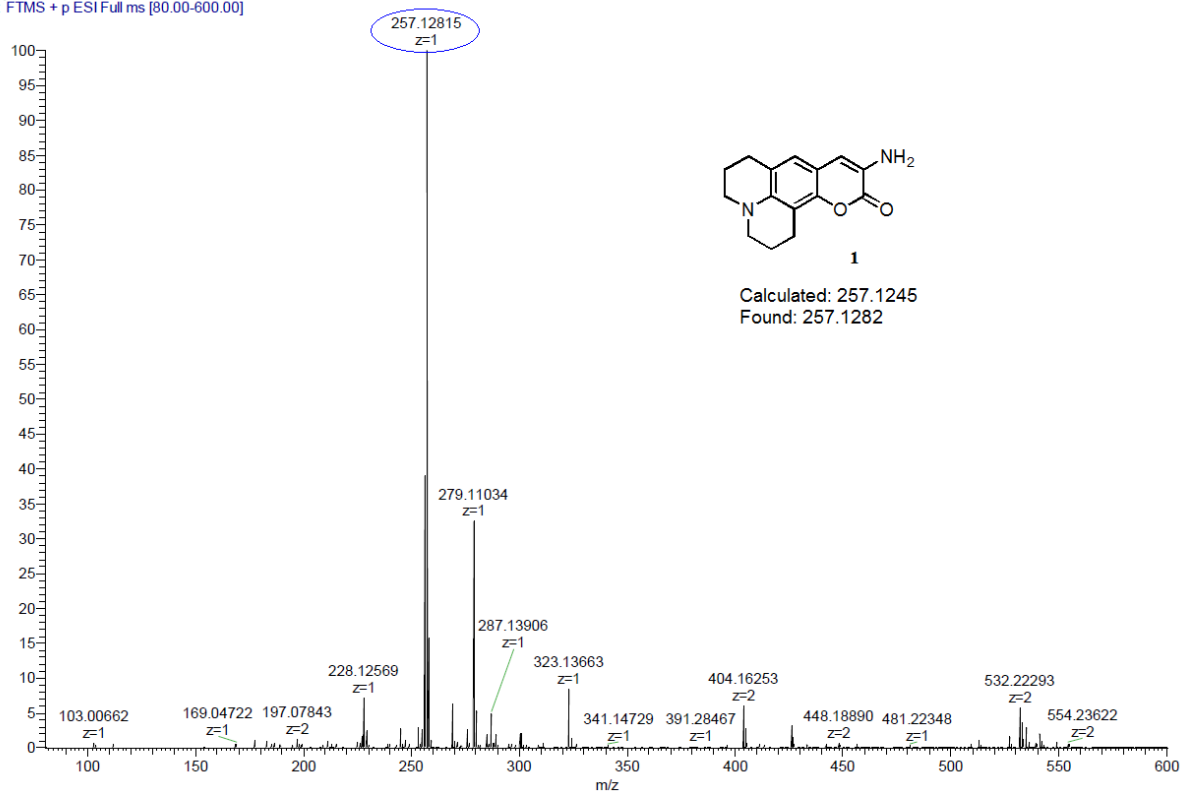
Figure S1. HRMS (ESI+): **1**

Figure S2. HRMS (ESI+): **2**

285.15943
z=1

307.14166
z=1

270.13620
z=1

256.15703
z=1

315.17034
z=1

446.20940
z=2

103.00663
z=1

169.04722
z=1

197.07843
z=2

383.12799
z=2

413.26646
z=1

499.27190
z=2

531.38673
z=1

591.29421
z=1

Calculated: 285.1558
Found: 285.1594

3

m/z
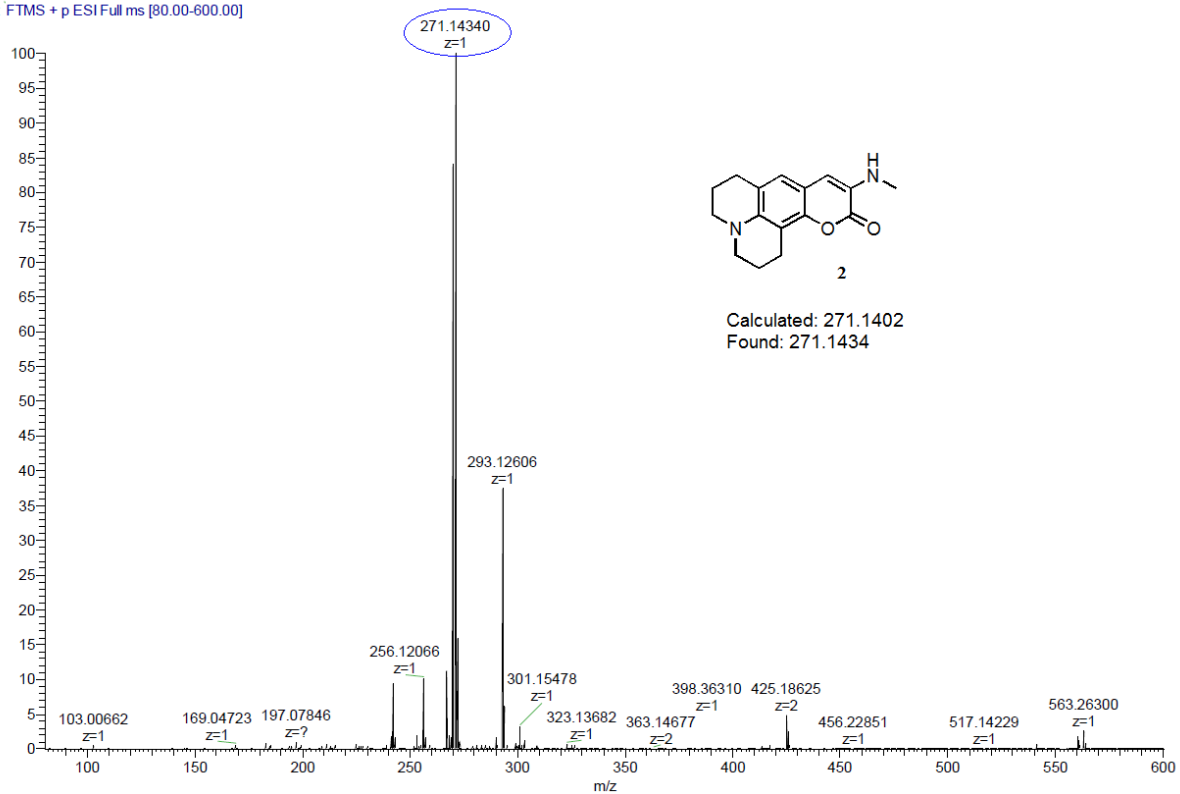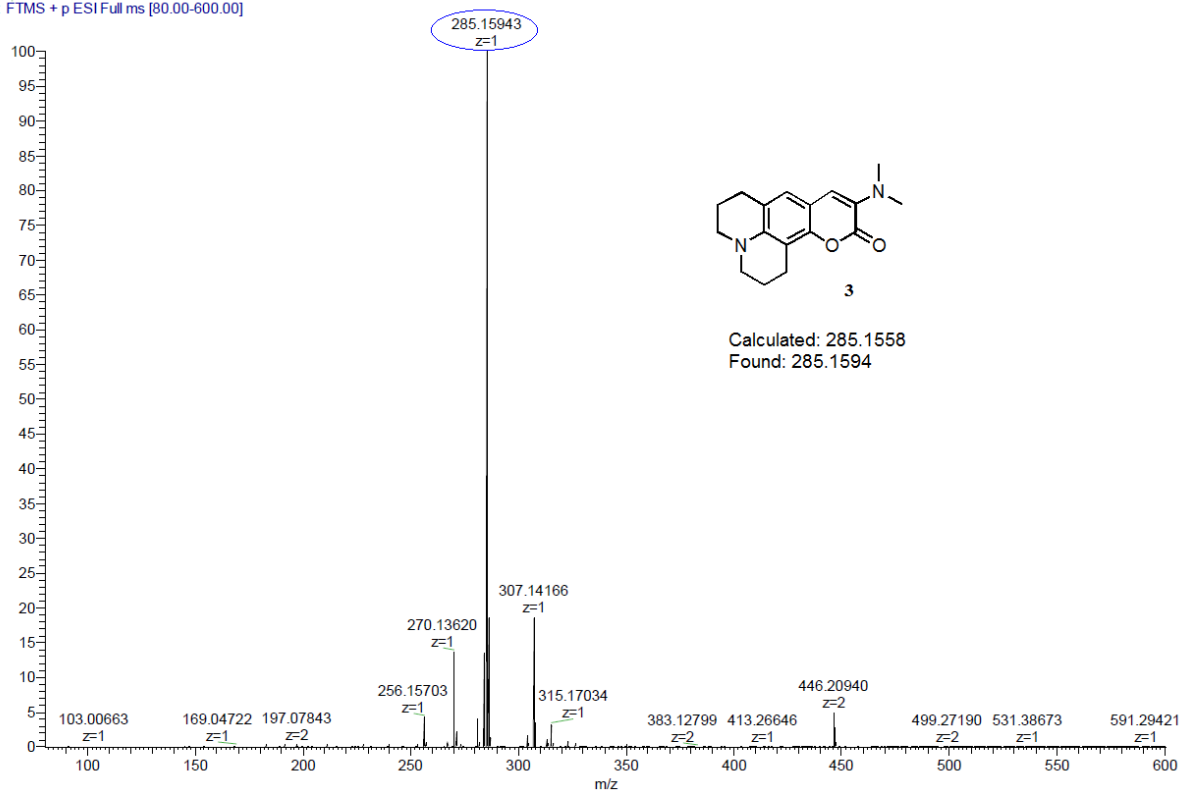
Figure S3. HRMS (ESI+): **3**

1.6. NMR Spectroscopy
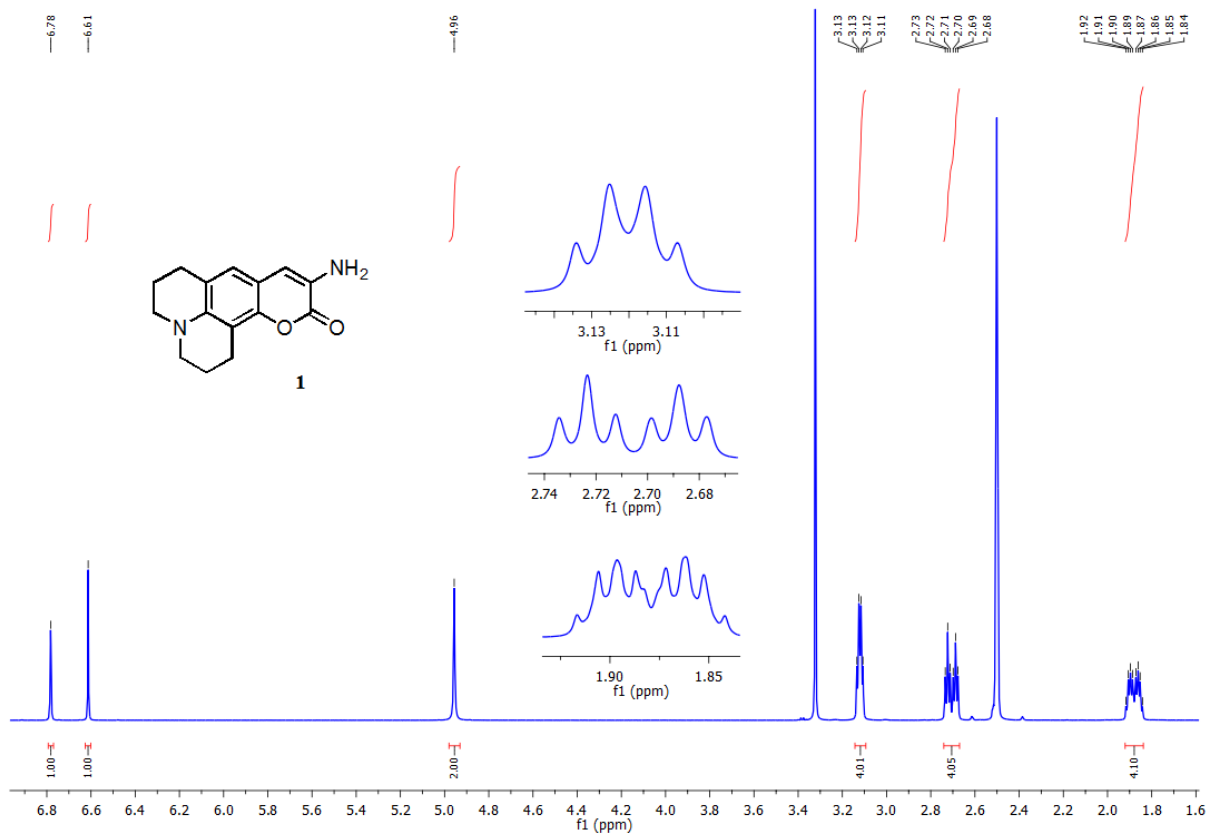
Figure S4. ^{1}H NMR (600 MHz, DMSO-d_6): **1**
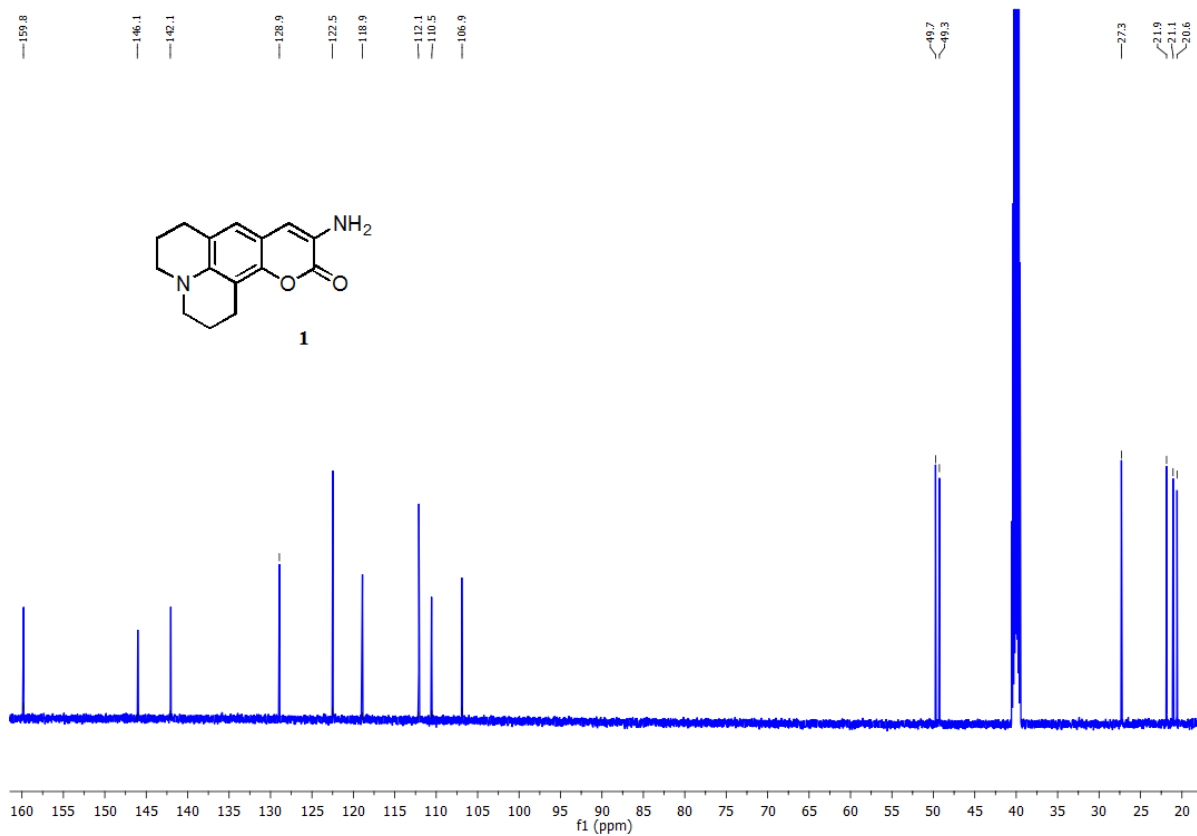
Figure S5. ^{13}C NMR (151 MHz, DMSO-d_6): **1**
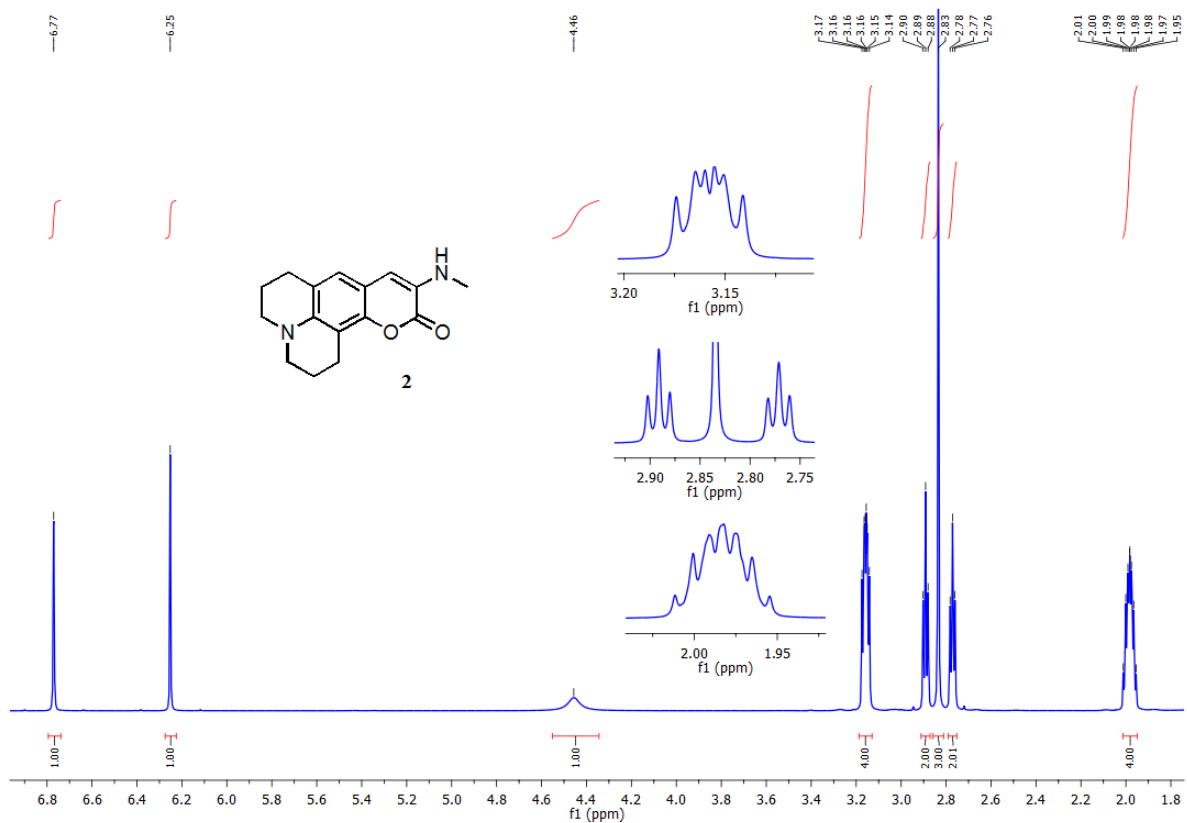
Figure S6. ^{1}H NMR (600 MHz, CDCl$_3$): **2**
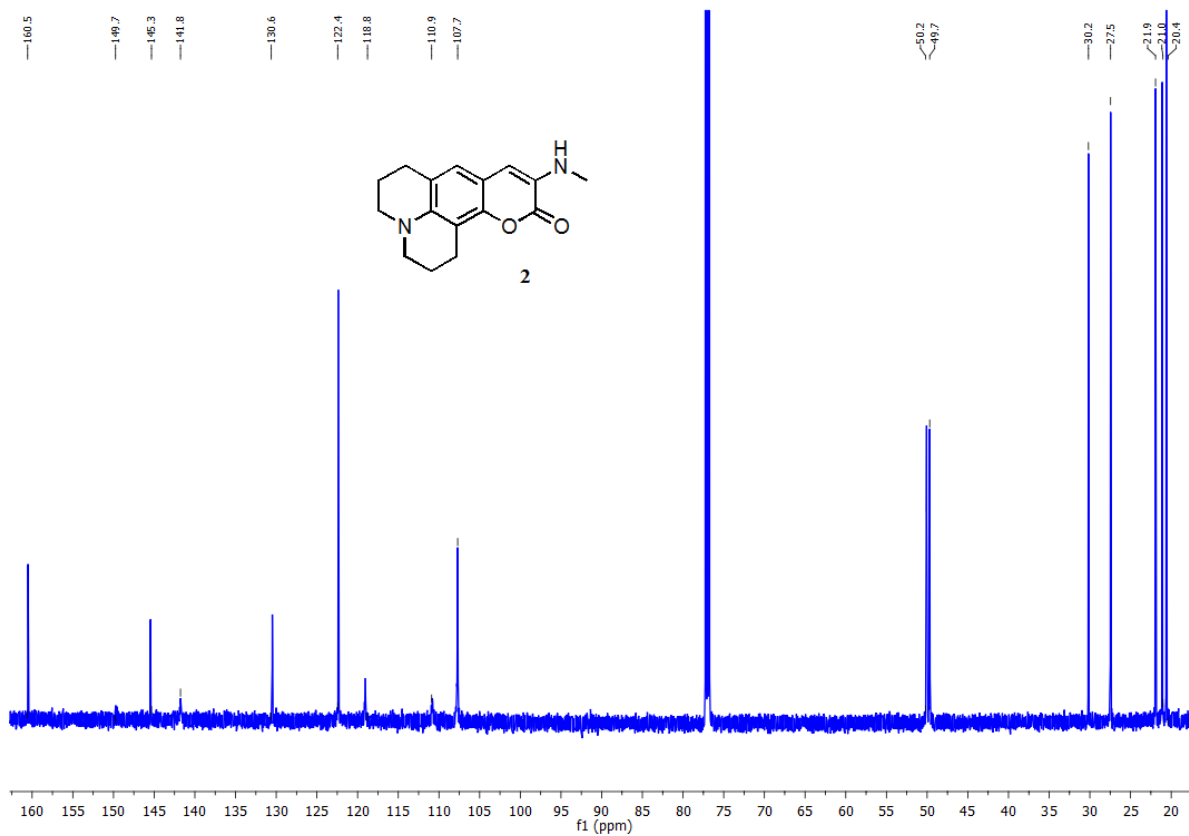
Figure S7. ^{13}C NMR (151 MHz, CDCl$_3$): **2**
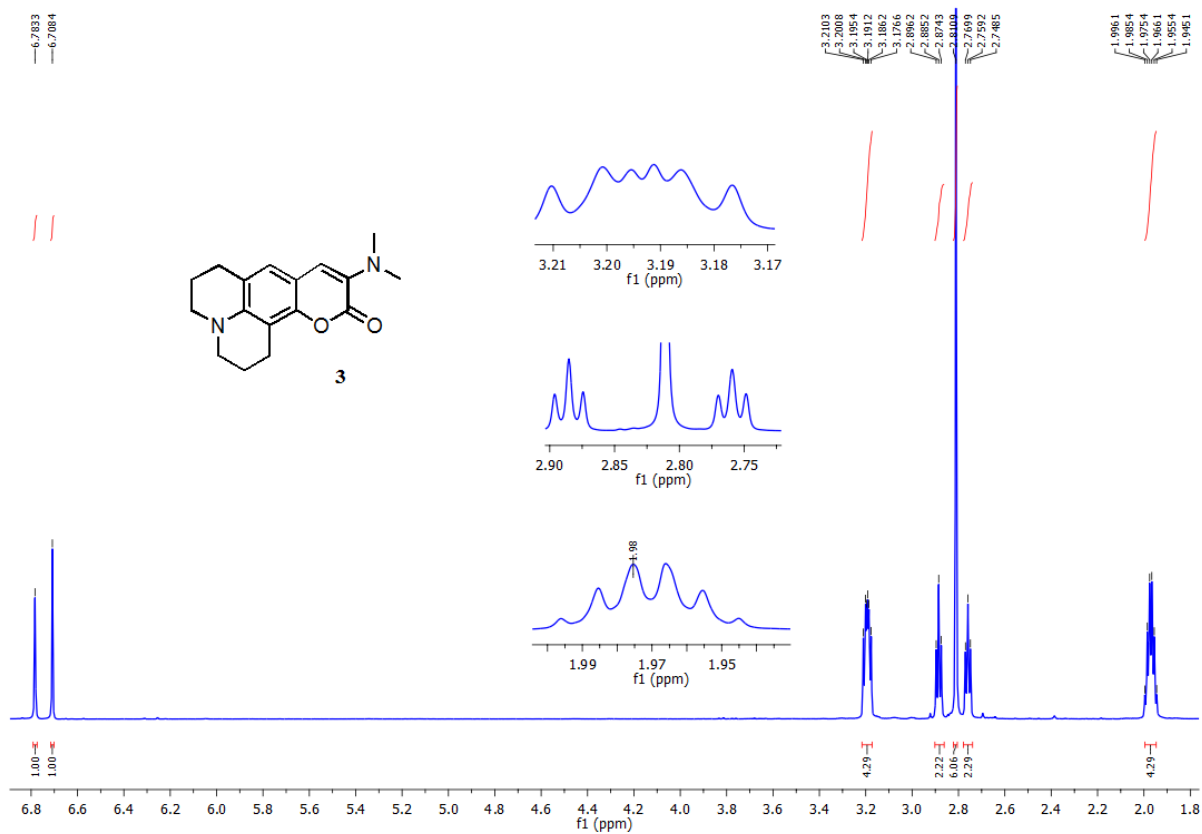
Figure S8. ^{1}H NMR (600 MHz, CDCl$_3$): **3**
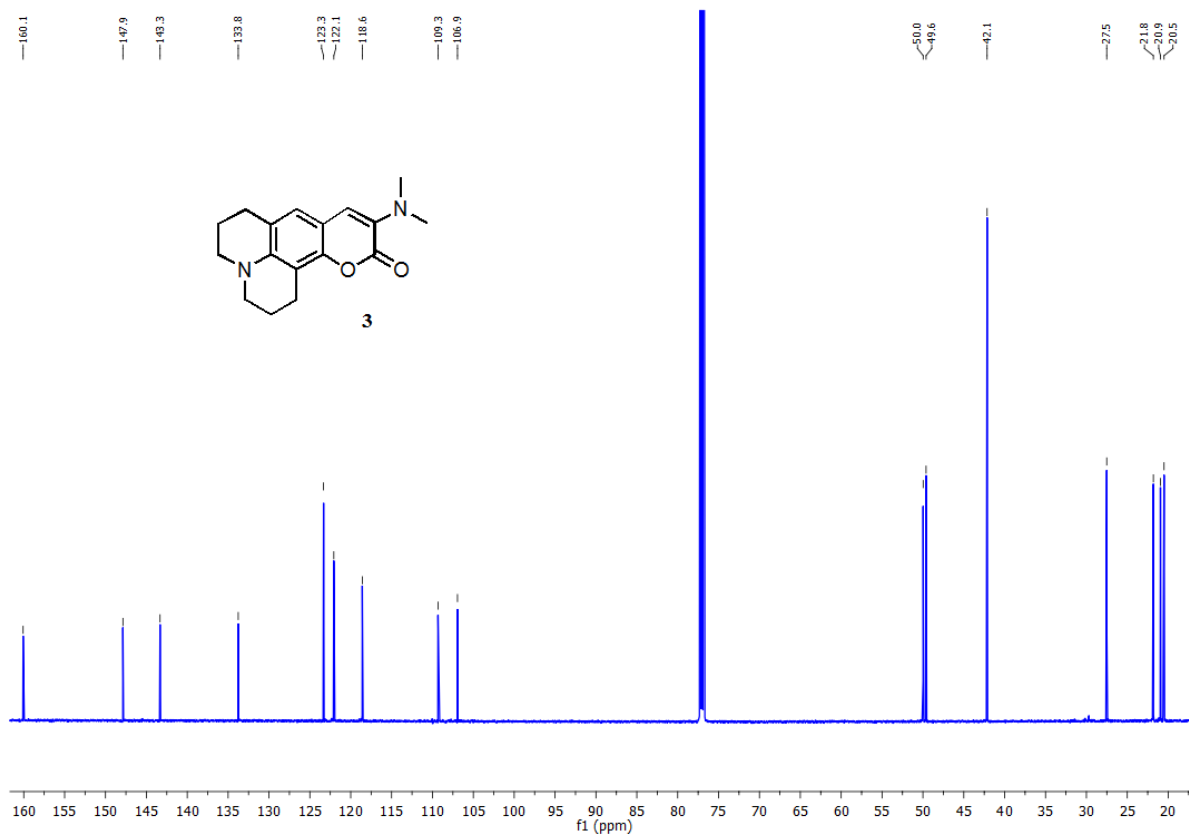
Figure S9. ^{13}C NMR (151 MHz, CDCl$_3$): **3**
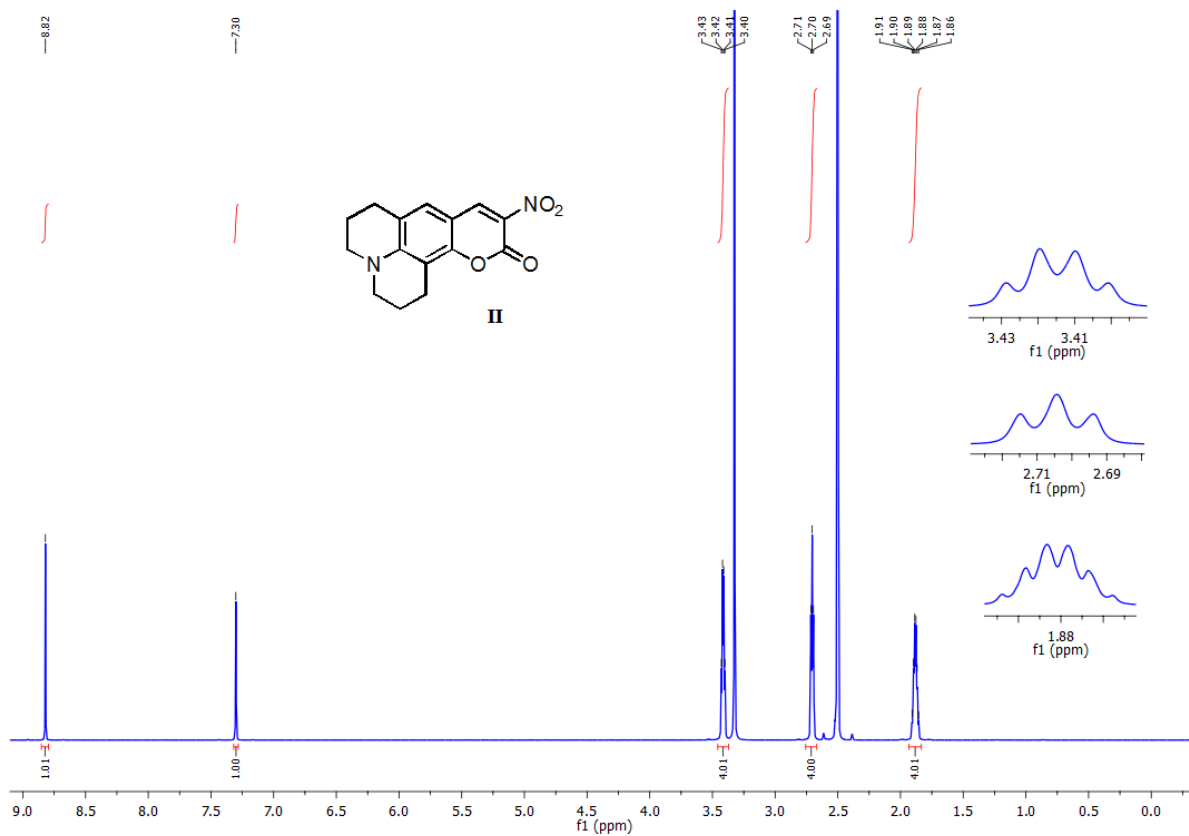
Figure S10. ^{1}H NMR (600 MHz, DMSO-d_6): **II**
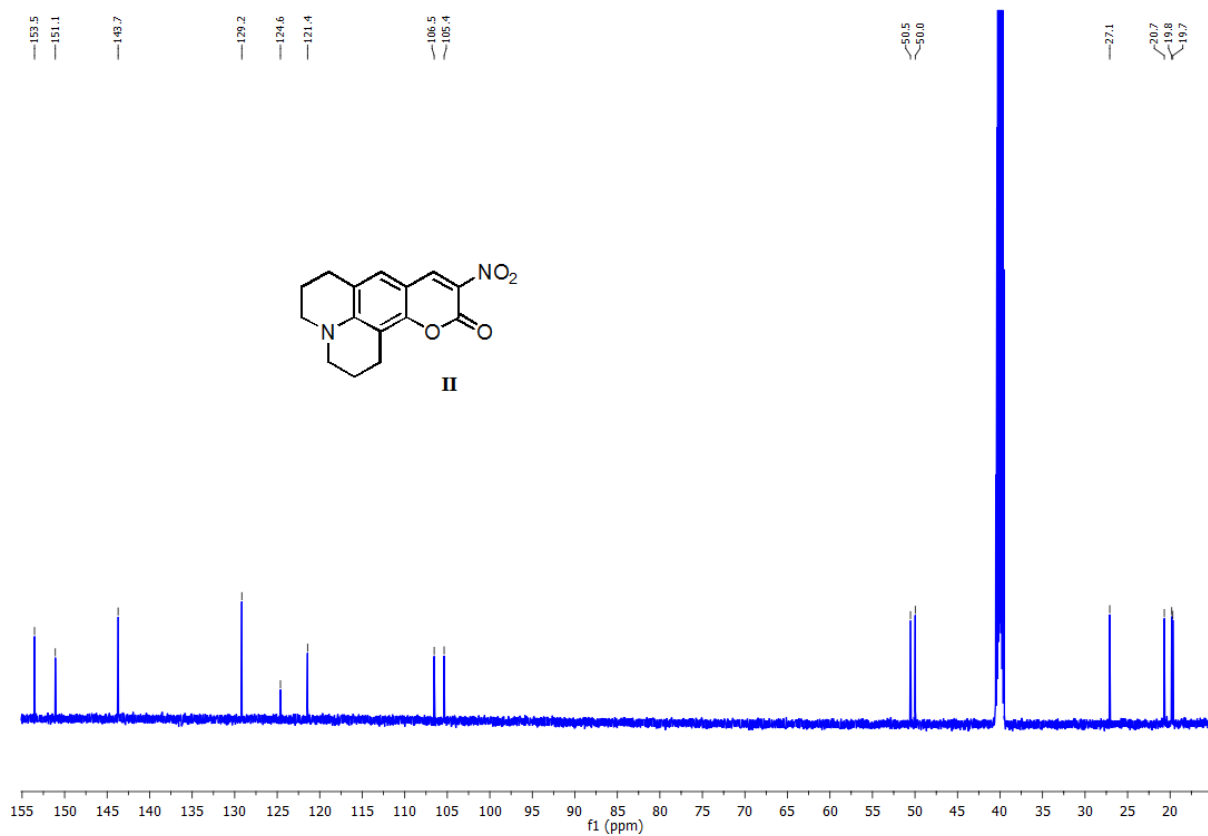
Figure S11. ^{13}C NMR (151 MHz, DMSO-d_6): **II**
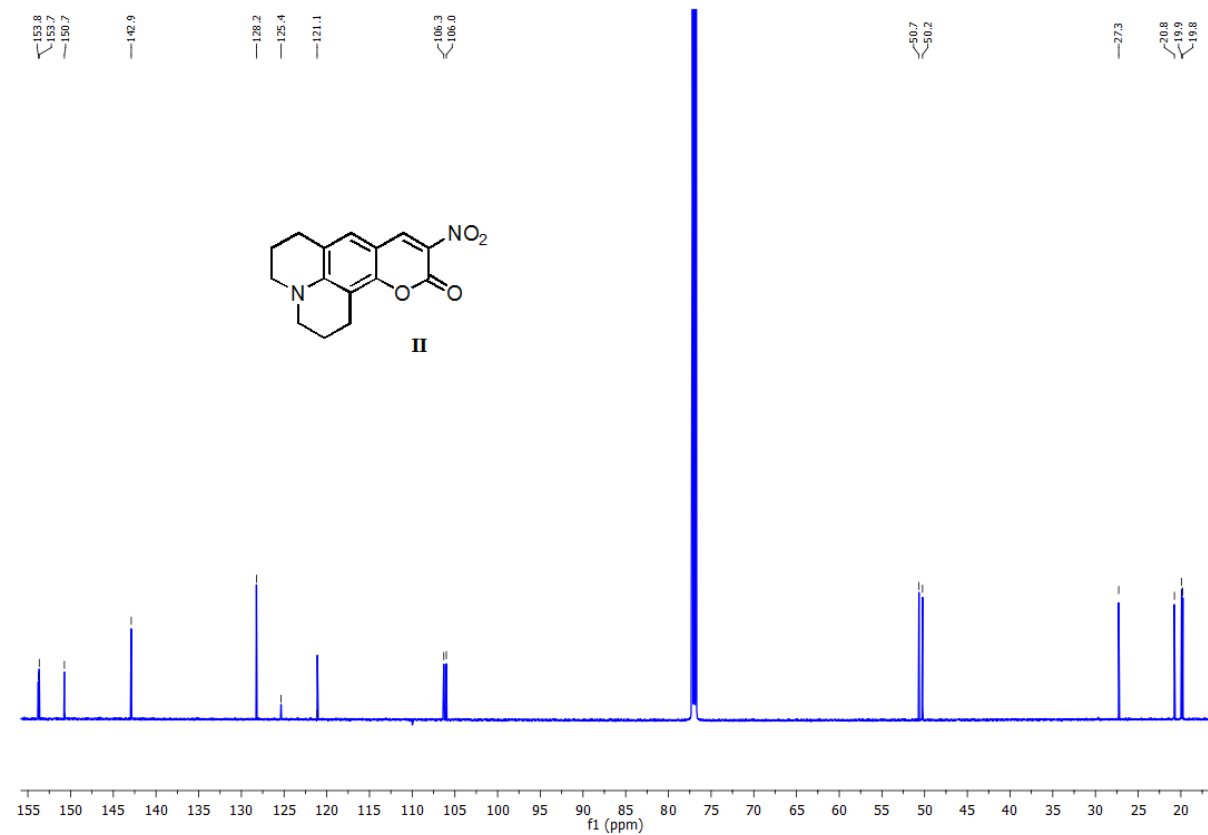
Figure S12. ^{13}C NMR (151 MHz, CDCl$_3$): **II**
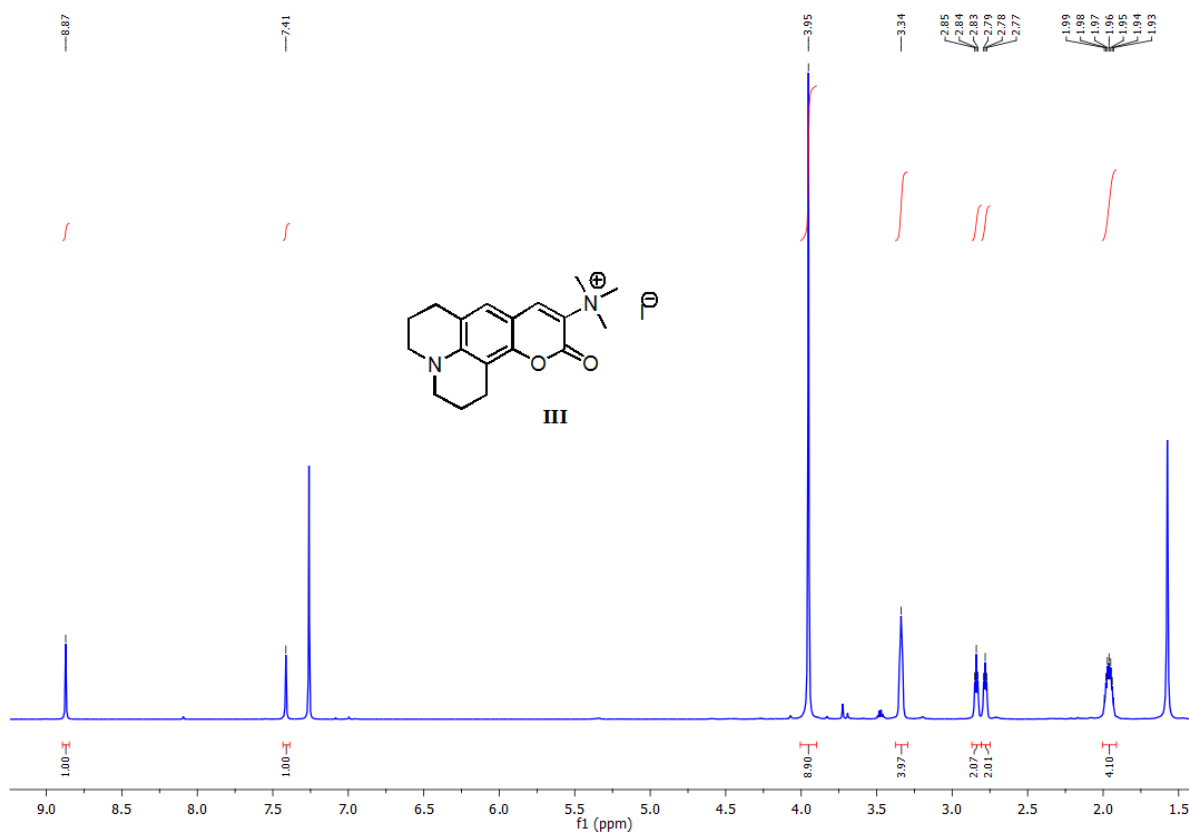
Figure S13. ¹H NMR (600 MHz, CDCl₃): **III** (crude)
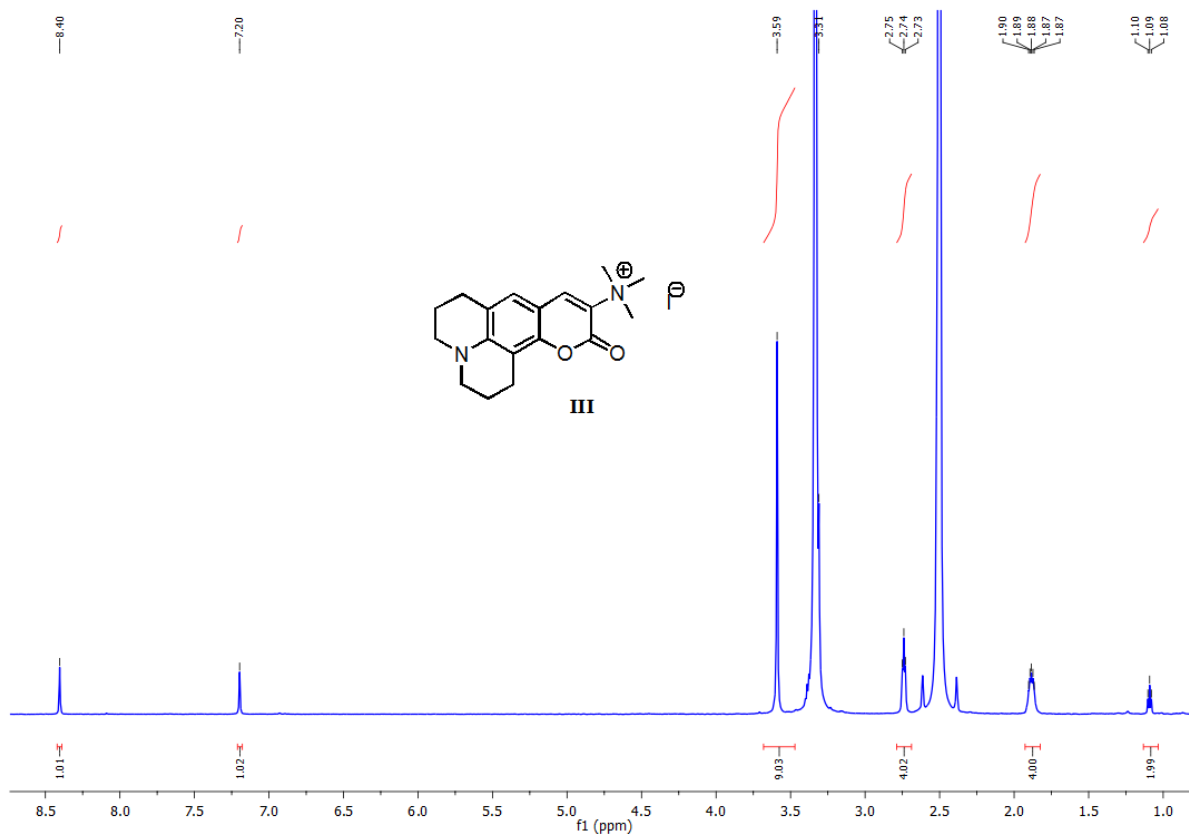
Figure S14. ¹H NMR (600 MHz, DMSO-d_6): **III** (crude)
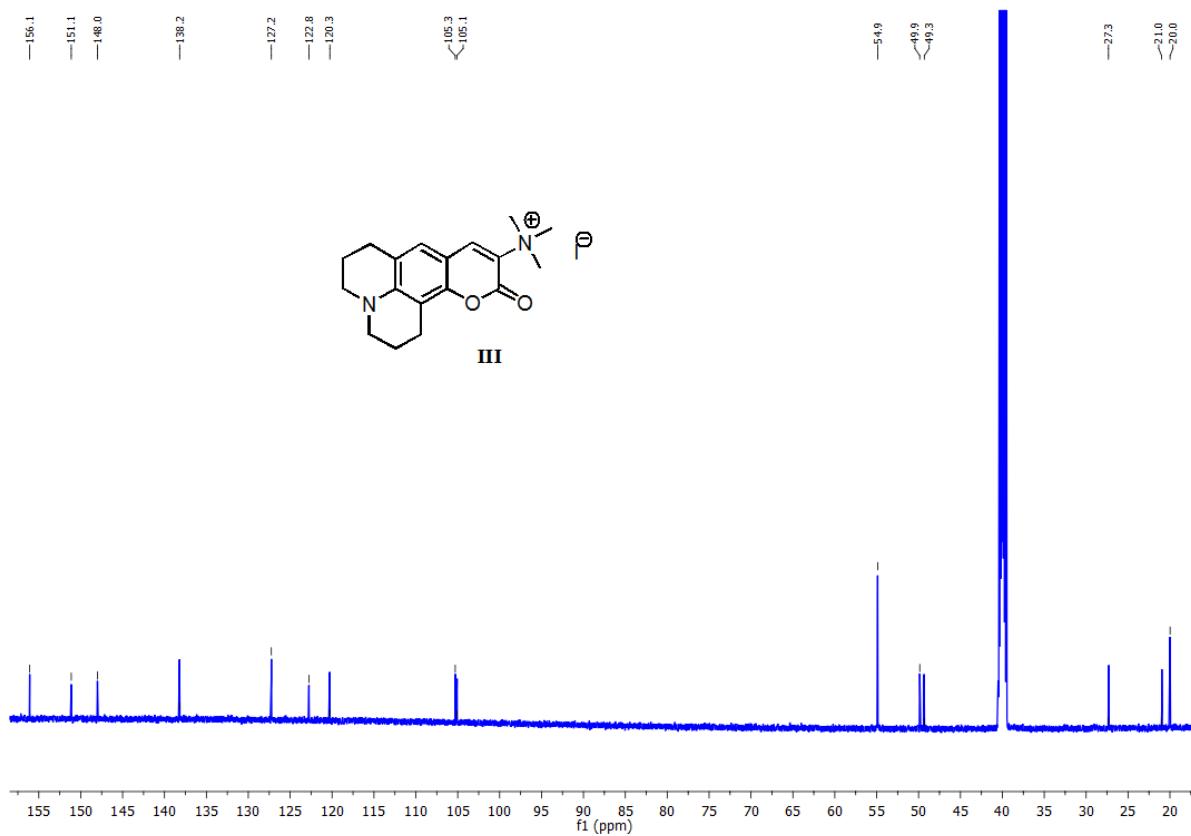
Figure S15. ^{13}C NMR (151 MHz, DMSO-d_6): **III** (crude)
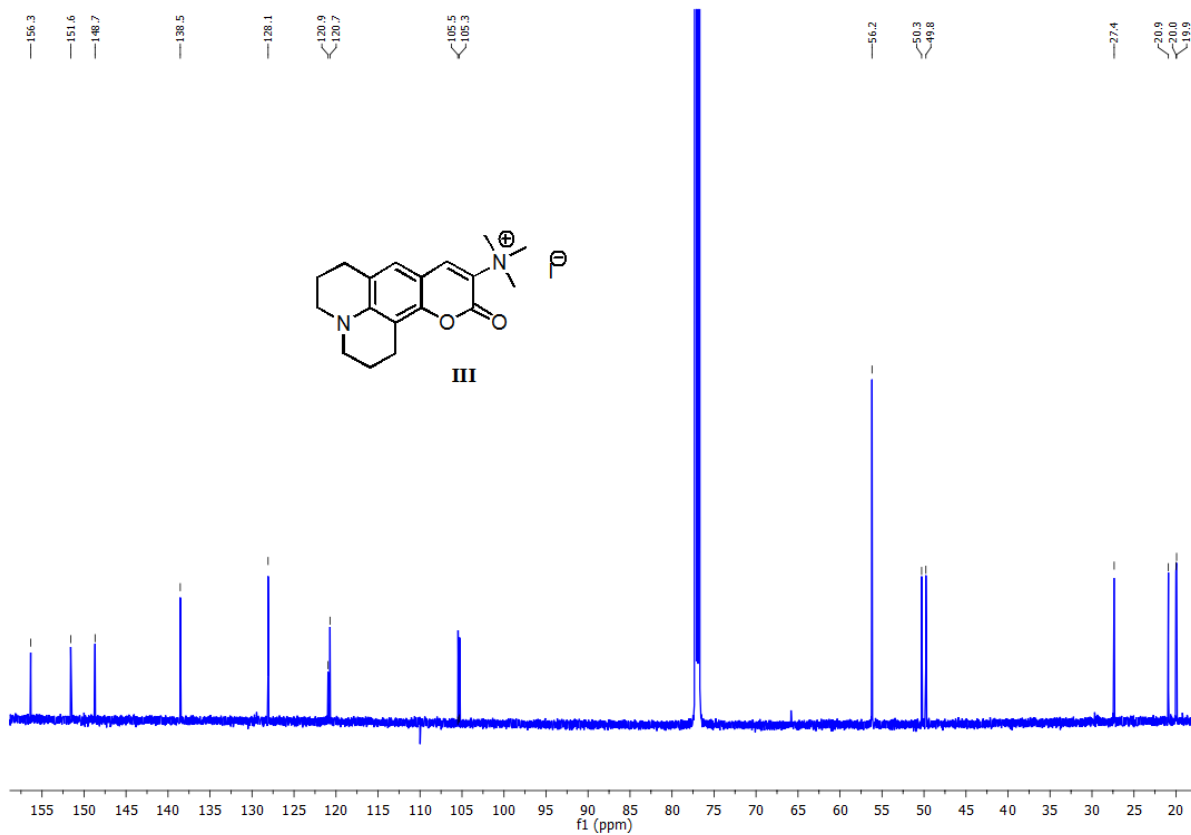
Figure S16. ^{13}C NMR (151 MHz, CDCl$_3$): **III** (crude)

1.7. IR Spectroscopy
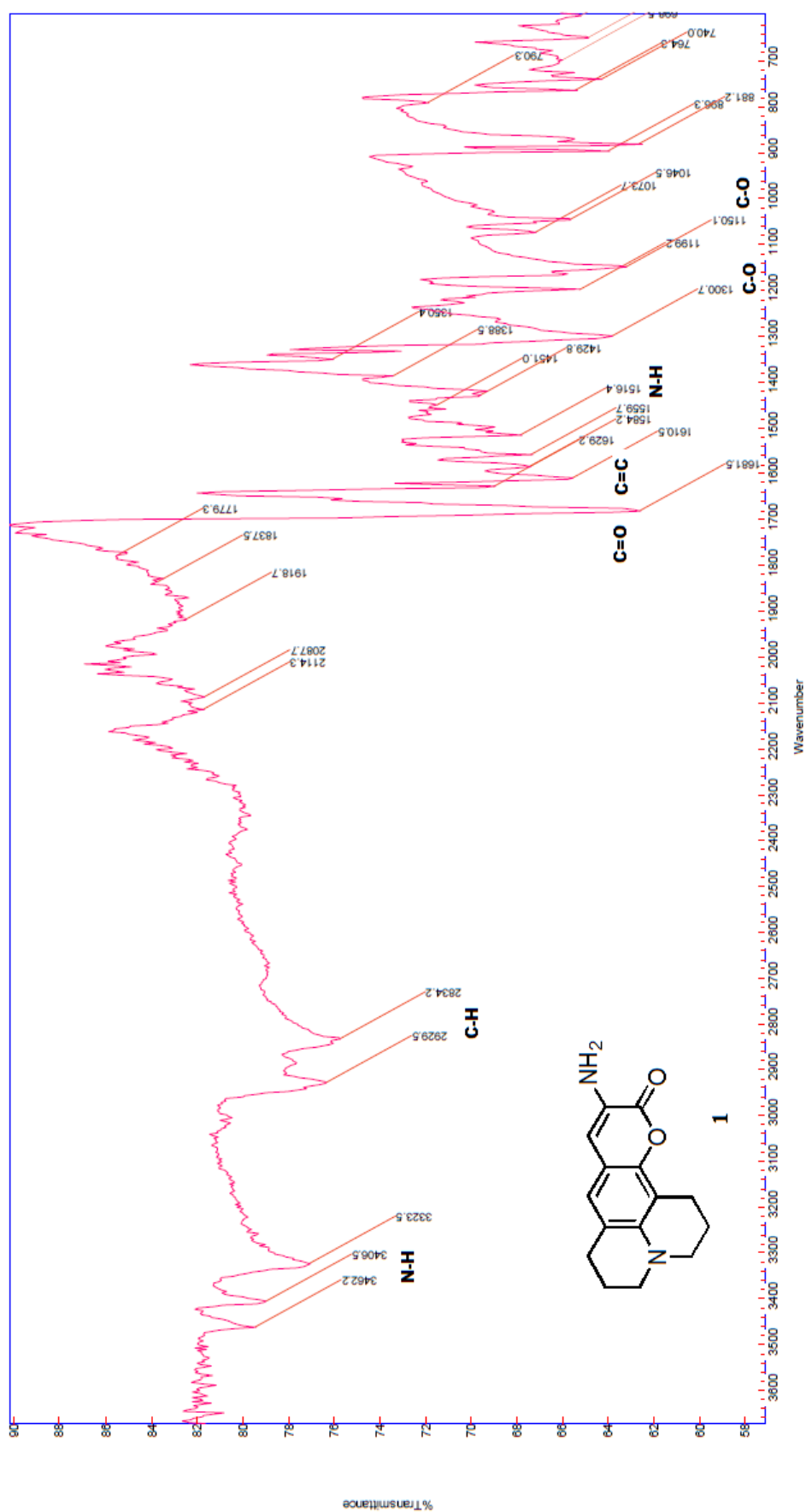
Figure S17. IR (ATR): **1**
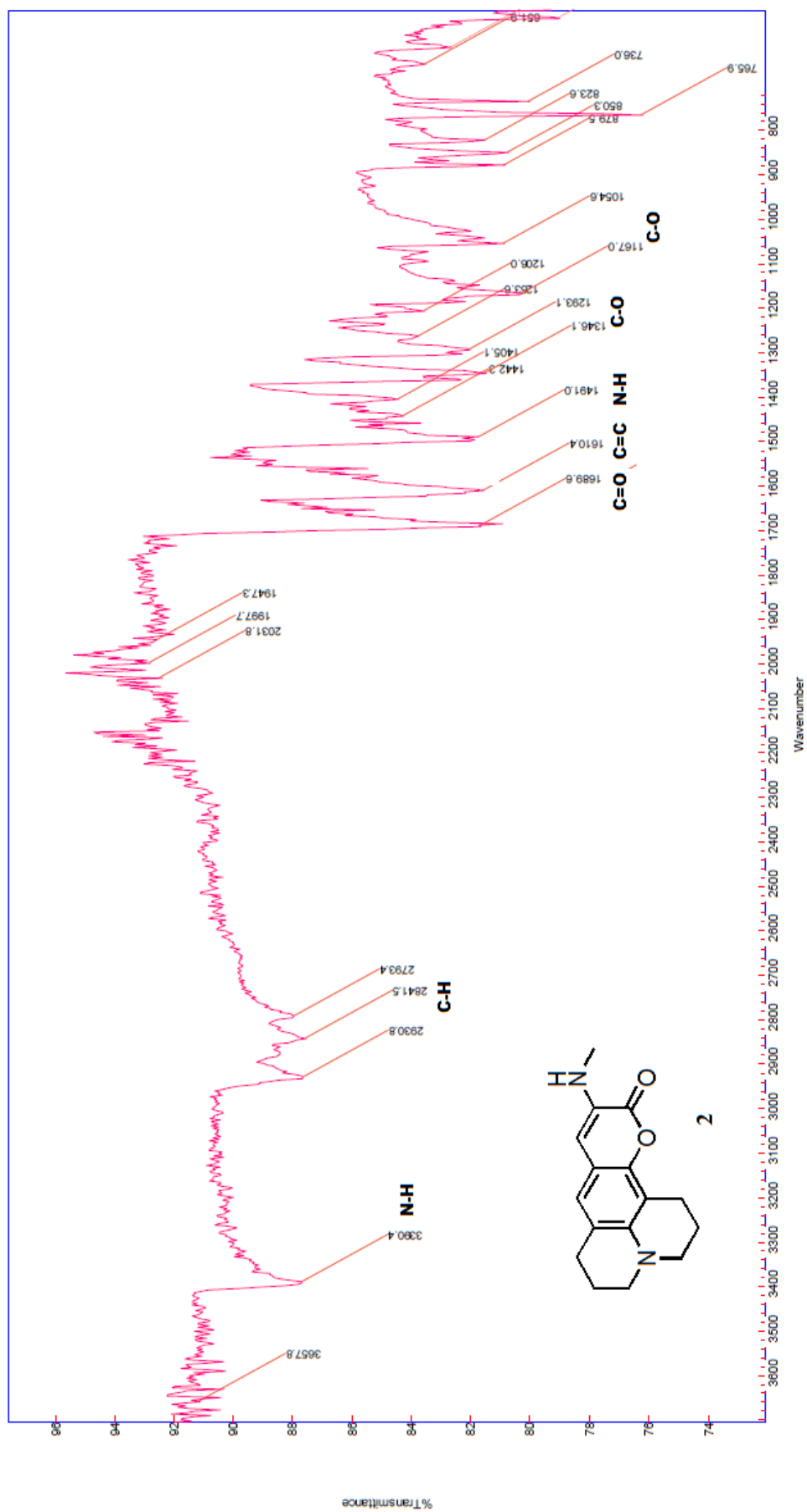
Figure S18. IR (ATR): **2**
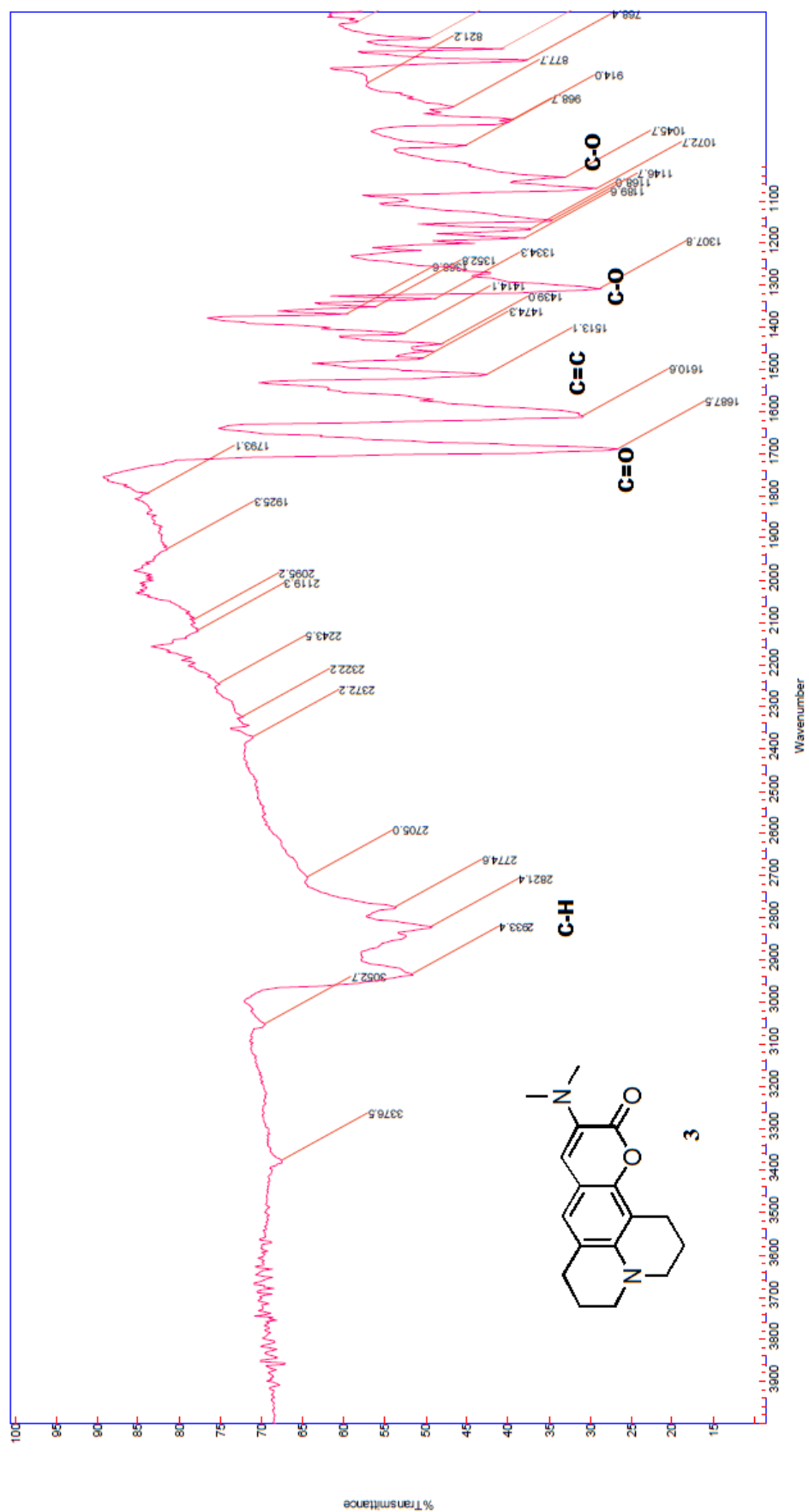
Figure S19. IR (ATR): **3**
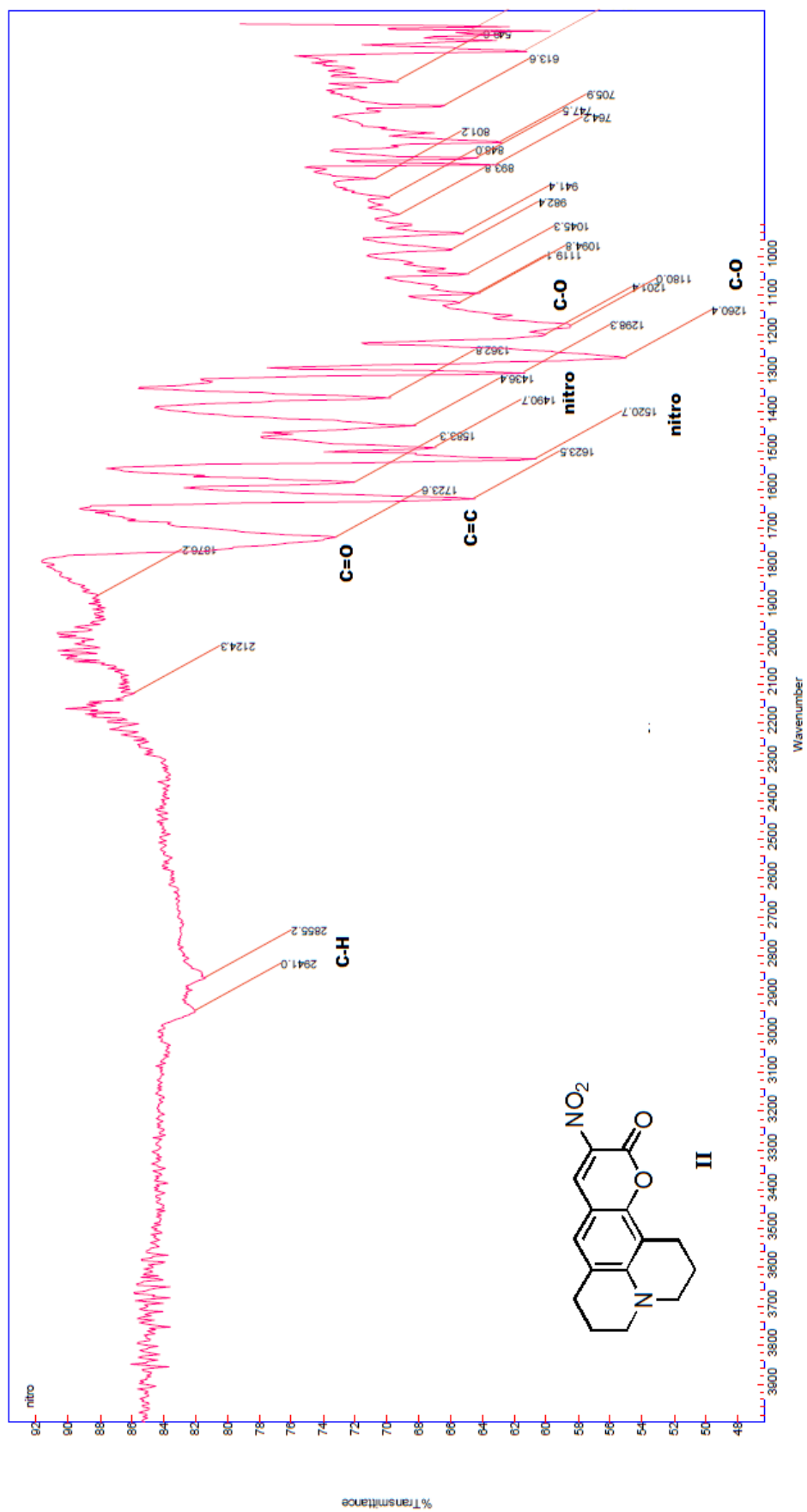
Figure S20. IR (ATR): **II**
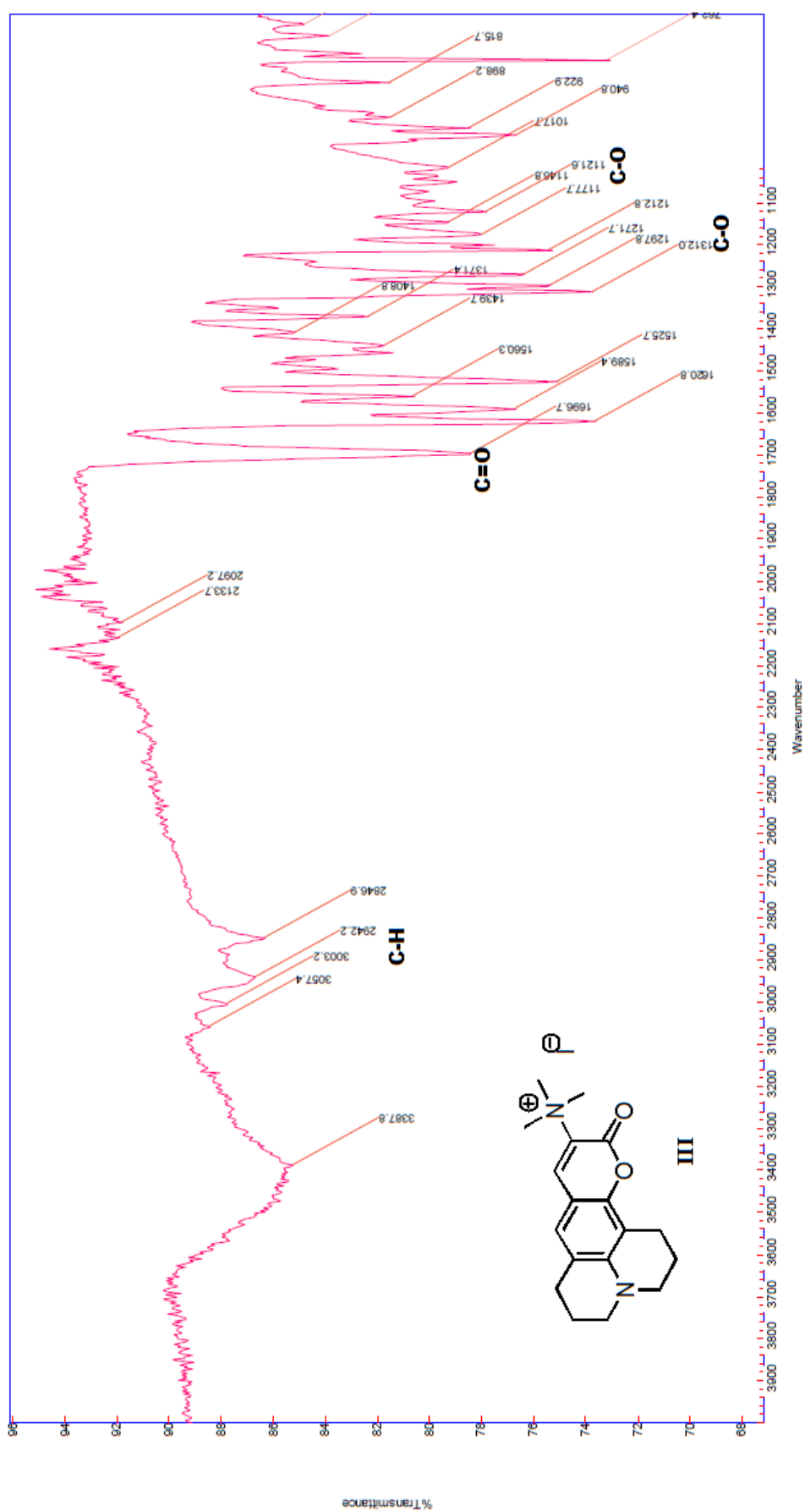
Figure S21. IR (ATR): **III** (crude)

1.8. References

[1]   Q. Sun, S.-H. Yang, L. Wu, W.-C. Yang, G.-F. Yang, *Anal. Chem.*, 2016, **88**, 2266. doi:10.1021/acs.analchem.5b04029.

[2]   M. Tajbakhsh, R. Hosseinzadeh, H. Alinezhad, S. Ghahari, A. Heydari, S. Khaksar, *Synthesis (Stuttg).,* 2011, 490. doi:10.1055/s-0030-1258384.

[3]   N.D. V Wilson, J.A. Joule, *Tetrahedron*, 1968, **24**, 5493. doi: 10.1016/0040-4020(68)88147-5.

2. pH Titration

2.1. Titration experiments

The standard pH titrations on studied coumarin probes **1**, **2**, and **3** (50 µM) were performed in aqueous solution (H₂O:DMSO mixture; 99:1 v/v). Samples were firstly dissolved in DMSO ($5×10^{-3}$ M) and 50 µL was then added to a buffer solution (Britton-Robinson, universal buffer solution I, 5 mL) of adjusted pH. The pH of the solutions was measured with Laboratory pH Meter WTW inoLab 720. Absorption and emission spectra of prepared final solutions were recorded with the increase in pH value. Corresponding pK_a values were determined from the x_0 point of sigmoidal fit of experimentally obtained fluorescence intensity dependence on pH.

2.2. pK_a determination of coumarin **1**

10-Amino-2,3,6,7-tetrahydro-1H,5H-quinolizino[9,1-gh]coumarin (**1**)
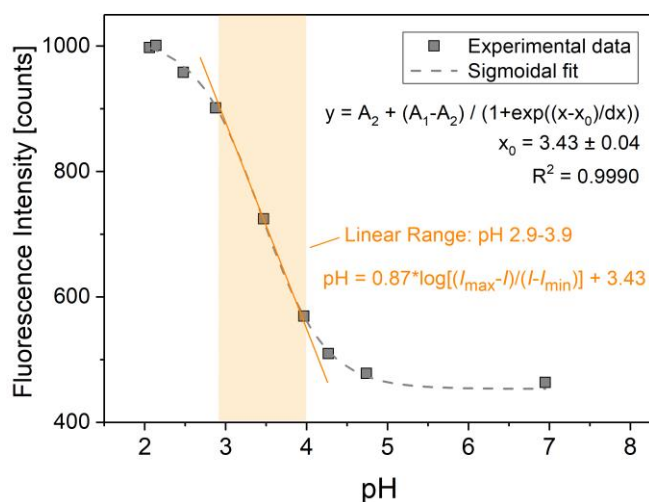
Figure S22. Sigmoidal fit of fluorescence intensity dependence of cpd **1** on pH ($\lambda_{exc} = \lambda_{abs}$ at pH=1.8; pK_a = x_0; I – fluorescence intensity; I_{max} – maximum fluorescence intensity; I_{min} – minimum fluorescence intensity).

2.3. Anti-interference capacity of the studied probe **1**
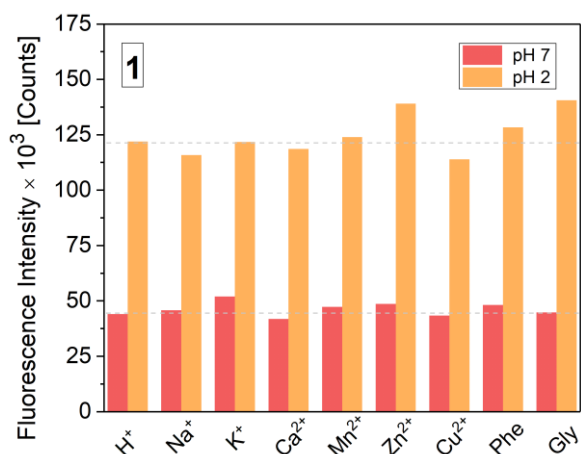
Figure S23. Fluorescence response at 520 nm of studied probe **1** in water in the presence of different metal ions and biological relevant species at pH 2.0 and 7.0 (Gly – glycine; Phe – phenylalanine; Concentrations: $[Na^+] = [K^+] = 150$ mM, $[Ca^{2+}] = 10$ mM, $[Mn^{2+}] = [Zn^{2+}] = [Cu^{2+}] = 0.2$ mM and $[Phe] = [Gly] = 1$ mM).

2.4. Possibility of determination of acidic pH in real juice sample
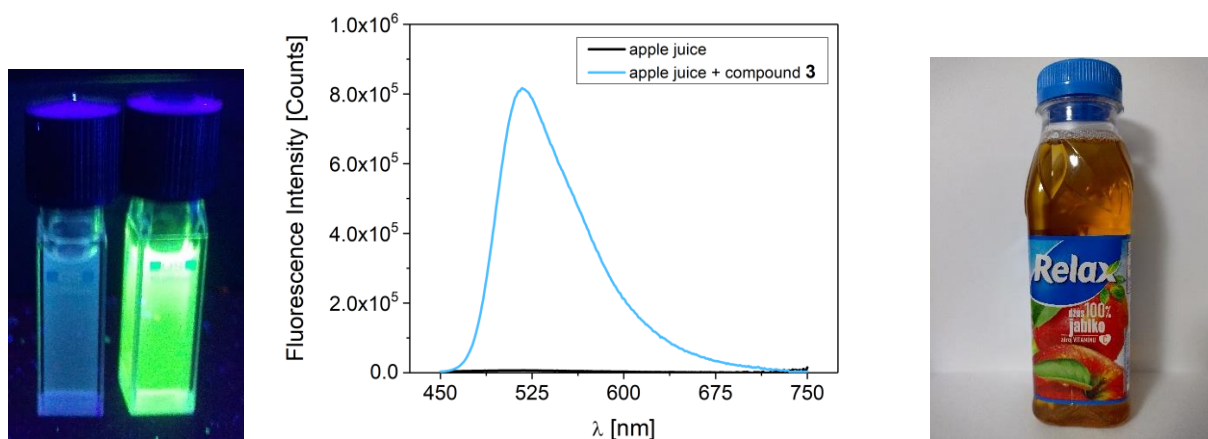
Figure S24. Possibility of determination of acidic pH in real apple juice sample: (Left) Fluorescence of juice sample without and with fluorescent probe **3**, respectively, under 365 nm UV light irradiation. (Middle) Corresponding fluorescence spectra at 430 nm excitation. (Right) Juice sample (pH ~ 3.5).

3. Photochemical Study

3.1. General Conditions

Electronic absorption spectra were collected on an Agilent 8453 diode array spectrophotometer (Hewlett Packard, USA). The H_2O:DMSO solvent mixture (99:1 v/v) was used as a solvent for all photochemical measurements of studied coumarin probes **1-3** (DMSO, Uvasol®, Sigma-Aldrich, St. Louis, MO, USA). Water was demineralized by a Pro-PS water purification system (Labconco, KansasCity, KS, USA) and kept highly demineralized by a circulation in a Simplicity deionization unit (Merck Millipore).

Solution fluorescence was measured in a 1 cm cuvette in a right-angle arrangement with FSP920/FLS1000 Photoluminiscence Spectrometers (Edinburgh Instruments, UK) or RF 6000 Spectrofluorometer (Shimadzu, Japan). Fluorescence lifetime (S_1 excited state lifetime) was determined on FLS1000 Photoluminiscence Spectrometer (Edinburgh Instruments, UK) using 448.2 nm picosecond pulsed diode laser excitation (EPL-450, Edinburgh Instruments, UK).

Transient absorption spectra were obtained on a LP980 Transient Absorption Spectrometer (Edinburgh Instruments; λ_{exc} = 355 nm – Nd/YAG laser).

3.2. Effect of pH on absorption and fluorescence spectra of compound 1
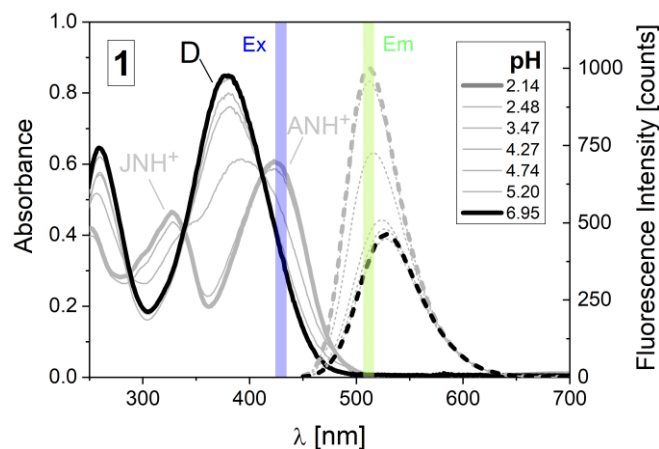
Figure S25. Evolution of absorption (solid line) and emission (dotted line) spectra of the studied coumarin probe **1** during pH titration experiments. Blue vertical line indicates the corresponding excitation wavelength, whereas green vertical line the position of fluorescence maximum. Letter D denotes absorption band of deprotonated (neutral) form; shortcuts JNH^+ and ANH^+ indicate absorption bands of protonated julolidine form and protonated amino form, respectively.

3.3. Excitation spectrum of compound 2
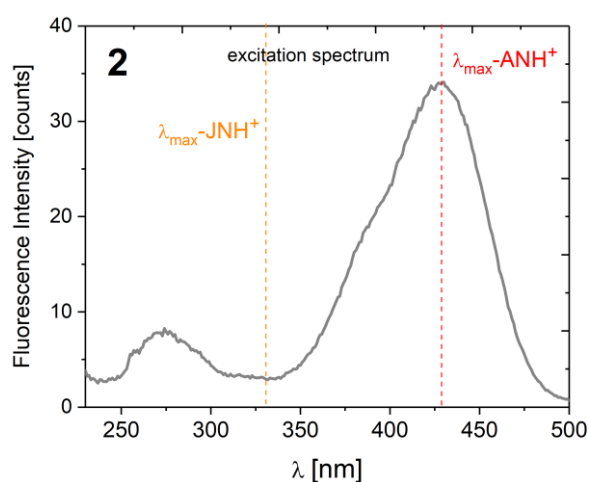
Figure S26. Excitation spectrum of **2** measured at pH = 1.8 (λ_{max}-JNH^+ - position of absorption maximum of the protonated julolidine form; λ_{max}-ANH^+ - position of absorption maximum of the protonated methylamino form).

3.4. Two Protonated Forms

Although determined pK_a values at 320 nm and 450 nm are almost the same (Fig. S27), the presence of only one protonated form cannot explain the appearance of absorption band at approximately 325 nm after "demethylation" of dimethylamino group in position 3 on coumarin skeleton (UV-Vis spectra of cpds **1** and **2** compared the spectrum of cpd **3**), nor the absence of contribution of this absorption band to overall fluorescence (excitation spectrum of cpd **2**). Moreover, calculated electronic spectra (which correlate nicely with the experimental ones) exclude the significant absorption of 3-amino protonated form (ANH$^+$) around 425 nm. On the contrary, they support the presence of julolidine protonated form (JNH$^+$) with main long-wavelength absorption band at approximately 325 nm.

To confirm our hypothesis of the presence of two prototropic forms, we carried out additional UV-Vis spectroscopy and ^{1}H NMR experiments. As shown in Figs. S28 and S31, whereas almost complete absence of absorption at approximately 325 nm (and simultaneous appearance of the ANH$^+$ absorption band) reflects in the presence of one set of signals in ^{1}H NMR spectrum, the appearance of the absorption band in this region leads to apparent addition of the second set of signals from the second protonated form (Fig. S29 top).
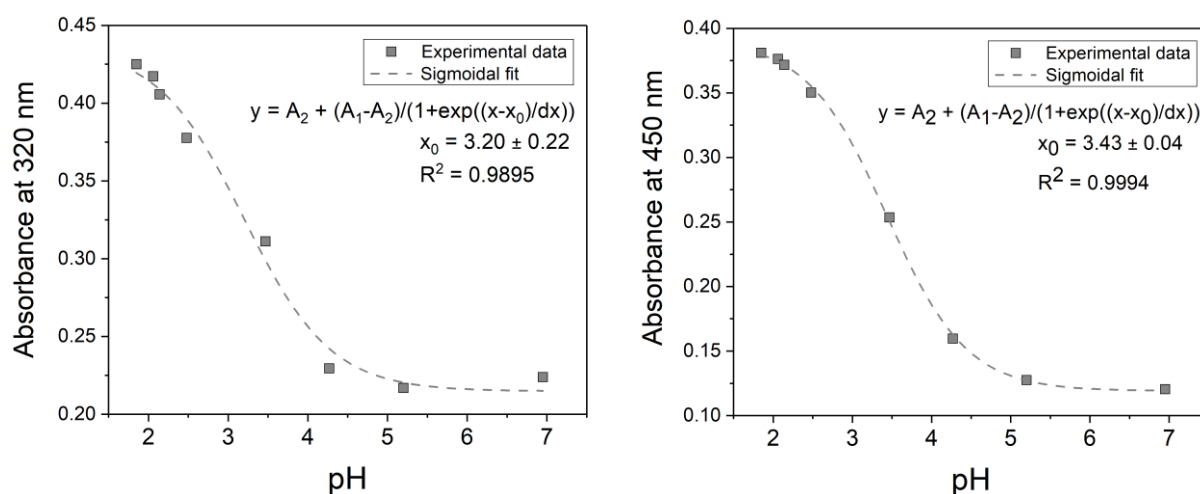
Figure S27. Sigmoidal fit of absorbance dependence of cpd **1** on pH (pK_a = x_0). (Left) Evolution of absorbance at 320 nm. (Right) Evolution of absorbance at 450 nm.
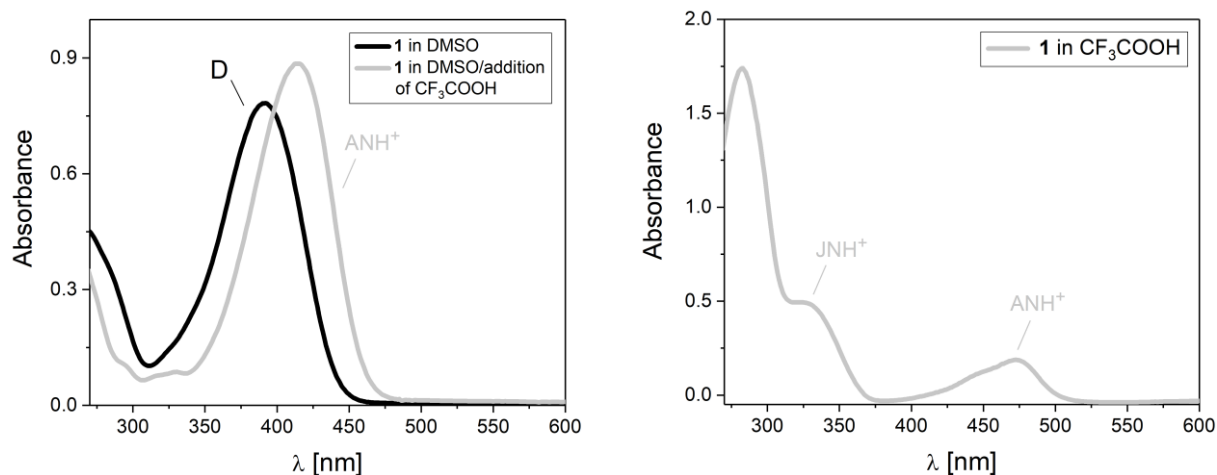
Figure S28. (Left) UV-Vis absorption spectrum of cpd **1** in DMSO before and after CF$_3$COOH addition; (Right) UV-Vis absorption spectrum of cpd **1** in CF$_3$COOH. Letter D denotes absorption band of deprotonated (neutral) form; shortcuts JNH+ and ANH+ indicate absorption bands of protonated julolidine form and protonated amino form, respectively.
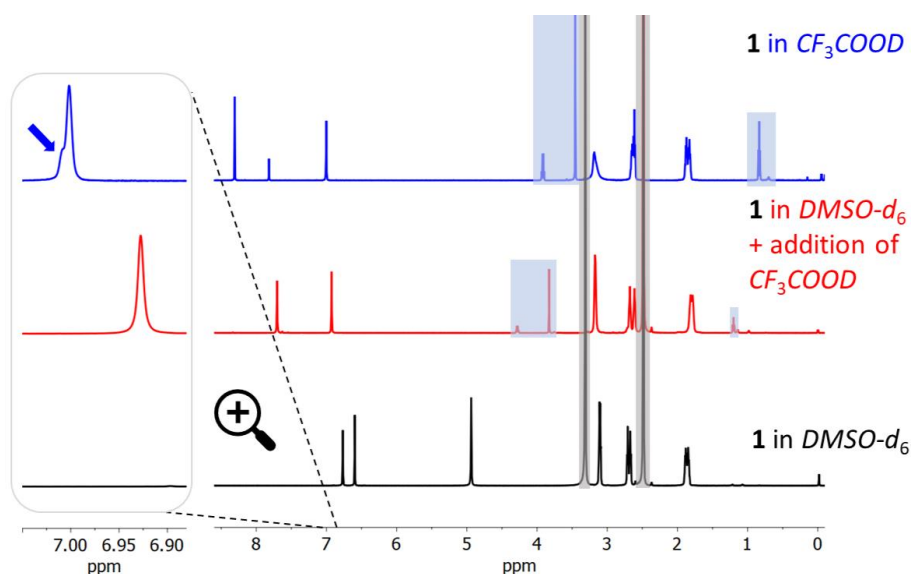
Figure S29. ^{1}H NMR spectrum of cpd **1** in DMSO-d_6 before (bottom) and after (middle) addition of CF$_3$COOD, and corresponding ^{1}H NMR spectrum of **1** in pure CF$_3$COOD (top) (the whole spectrum in CF$_3$COOD was shifted by -0.44ppm to facilitate signals´ comparison; gray and blue rectangles indicate solvent residual peaks and solvent impurities, respectively; impurities originated from CF$_3$COOD did not disappear from spectrum even after the CF$_3$COOD batch change).

3.5. Fluorescent Quantum Yields

Fluorescent quantum yields (Φ_F) of studied compounds were determined on a spectrofluorophotometer RF 6000 (Shimadzu, Japan) using the relative method (comparison to a published quantum yield standard) according to equation Eq. (1):

$$\Phi_{F(X)} = \Phi_{F(ST)} \left(\frac{Grad_X}{Grad_{ST}} \right) \left(\frac{\eta_X^2}{\eta_{ST}^2} \right) \tag{1}$$

where the subscripts X and ST refer to the sample and standard, Φ_F is the fluorescent quantum yield, Grad denotes the slope (gradient) of the plot of integrated fluorescence intensity against absorbance, and η is the refractive index of the solvent. Perylene in cyclohexane was used as a quantum yield standard ($\Phi_{F(Perylene)} = 0.94$ from reference [4]).
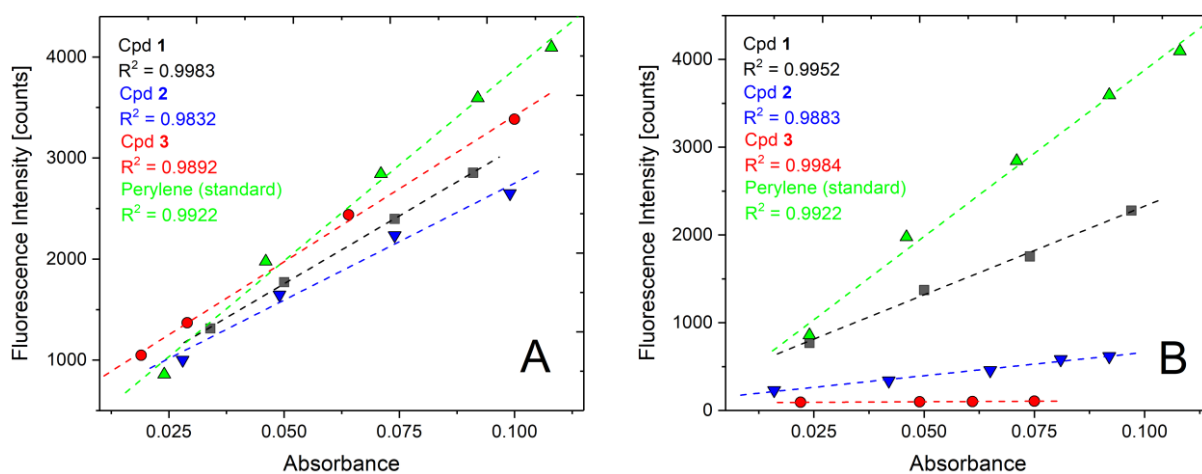
Figure S30. Plots of integrated fluorescence intensity against absorbance of studied coumarin probes **1**, **2** and **3** ($\lambda_{exc} = 410$ nm) in H_2O:DMSO mixture (99:1 v/v) measured at (A) pH = 1.90 and (B) pH = 7.68.

3.6. Nanosecond Laser Flash Photolysis
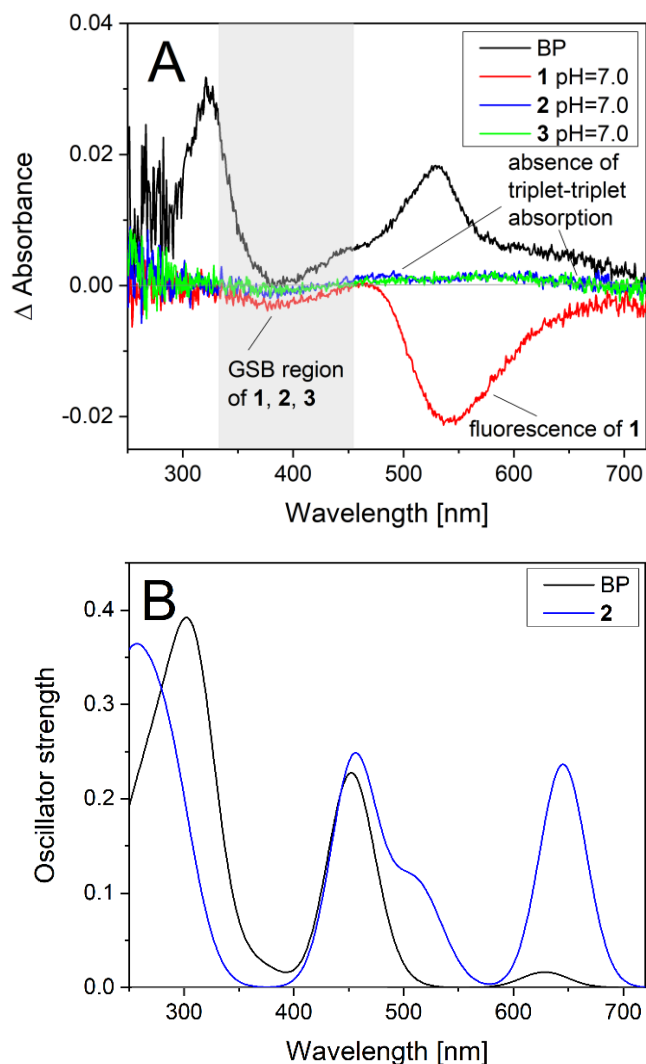
Figure S31. (A) Transient absorption spectra of neutral forms of studied coumarin probes **1**-**3** (pH = 7.00) in H_2O:DMSO 99:1 (v/v) and benzophenone (BP) in benzene (as standard) for comparison (GSB = Ground State Bleach). All samples were excited at λ_{exc} = 355 nm (Delay time: 0 ns).

(B) Theoretically predicted triplet-triplet absorption spectrum of cpd **2** and benzophenone (BP). Molecular geometry was optimized in the lowest triplet state at the CAM-B3LYP/def2TZVPP level of theory in water (SMD, continuum model). Next, 20 triplet excited states were calculated using TD-U-CAM-B3LYP/ def2TZVPP in water. Each excited state oscillator strength was broadened by a gaussian function with full width at half maximum (FWHM) set to 50 nm.

3.7. Stability of Fluorescence Signal
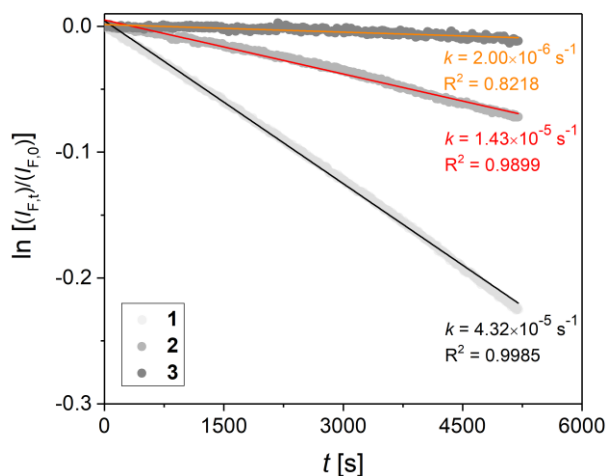
Figure S32. Stability of fluorescence signal of the studied probes at pH = 1 with determined rate constants k for signal decrease ($I_{F,0}$ and $I_{F,t}$ are fluorescence intensities at time zero and t, respectively).

As shown in Fig. S32, decrease in fluorescence signal of probe **3** is less than 1% per hour and thus indicates good stability of this probe even in the strongly acidic environment. Interestingly, systematic methylation of the amino group thus effectively tunes not only the fluorescence enhancement factor and the usable pH range of a probe, but also stability of fluorescence signal.

To investigate the contribution of photodegradation to the decrease in fluorescence signal, we determined the corresponding quantum yields of photodegradation ($\Phi_{photodeg}$) for probes **2** and **3** (Fig. S33) using Eq. (2):

$$\Phi_{photodeg} = \frac{\left(\frac{I_{F,0} - I_{F,t}}{I_{F,0}}\right) \times c_0}{\int_0^t I_a dt} \qquad (2)$$

where c_0 means the initial concentration of the probe (determined by UV-Vis spectroscopy – Lambert-Beer law) and $\int_0^t I_a \, dt$ is the overall absorbed light intensity by the probe (for details of I_a determination, please see reference [5]). Solutions of samples **2** and **3** were irradiated with four 405 nm LED diodes Thorlabs with individual optical power of 10 mW (overall incident light intensity $I_0 = 4.2 \times 10^{-5}$ mol dm^{-3} s^{-1} was determined in our previous paper; for details, please see reference [5]).

As shown in Fig. S33, probes **2** and **3** exhibit moderate photostability with the the photodegradation quantum yields lying in the range of 0.01-0.1% at pH = 3.5. Photostability of the studied probes is pH-dependent and decreases with the decreasing pH. Overall, photodegradation contributes significantly to the decrease in fluorescence signal intensity of the studied probes over time.
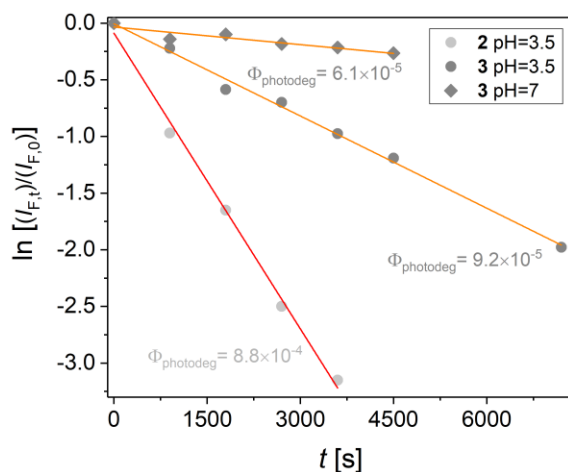
Figure S33. Photostability of the studied probes **2** and **3** represented by corresponding photodegradation quantum yield ($\Phi_{photodeg}$) and the influence of pH change on the photostability of probe **3** ($I_{F,0}$ and $I_{F,t}$ are fluorescence intensities at time zero and t, respectively).

3.8. References

[4]   I.B. Berlman, *Handbook of Fluorescence Spectra of Aromatic Molecules*, Academic Press, N.Y.2, 1965; https://books.google.sk/books?id=gqkaAAAAMAAJ.
[5]   B. Mravec, J. Filo, K. Csicsai, V. Garaj, M. Kemka, A. Marini, M. Mantero, A. Bianco, M. Cigáň, *Phys. Chem. Chem. Phys*, 2019, **21**, 24749. doi:10.1039/c9cp05049c.

4. Quantum-Chemical Calculations

4.1. Methodology

Molecular geometry of all studied probes was optimized at the CAM-B3LYP[5] level of theory, using def2-TZVPP[6] basis set and SMD[7] continuum solvation model. Local minimum character of obtained structure was confirmed by vibrational frequency calculation, always leading to real-value frequencies. To further precise the electronic energies we employed DLPNO-CCSD(T)[8] method with def2-TZVPP basis set. Electronic excitation energies were calculated using TD-CAM-B3LYP method, a generally good choice for both local and charge transfer states. Solvation effects on the excited states were described by the linear-response non-equilibrium solvation model (SMD, water solvent) for absorption spectra and as equilibrium solvation for emission. *Ab initio* methods CIS(D)[9] and CC2[10] were used to calculate excitation energies in the gas phase, which was corrected for the solvent effects from CAM-B3LYP calculation.

Minimal energy conical intersection (MECI) is a minimum of the set of points where energy of the ground and excited (S_1 in our case) states are near degenerated. Such a points are necessary photochemical funnels through which the population of excited could be deactivated without emission.[11] We attempted search for such a point from the Franck-Condon geometry both at the conventional TD-CAM-B3LYP methodology, which breaks near MECI, and using spin-flip version[12] which, due to triplet reference, works also in the MECI region. In the latter case the PBE0 functional was used. Fully converged geometries of the MECI were not obtained, yet the small energy difference between states (less than 0.1 eV) allow us to make qualitative conclusions regarding the type of molecular deformation necessary to reach MECI (see Fig. S34).

Fluorescence emission rate and the intersystem crossing rate were calculated in ORCA 5.0 software[13] using path integral approach[14] CAM-B3LYP functional and CPCM solvation model. Smaller, def2-SVP basis set was used in this case, since we applied Hertzberg-Teller approximation, i.e. the transition dipole moments derivatives with respect to vibrational modes were calculated, leading to larger computational demands. Non-adiabatic coupling terms for each vibrational mode was calculated using 2021A version MOMAP software[15]. For the intersystem crossing rates, we found that second triplet state T_2 is close to the S_1 minimum, thus the rate to three spin sublevels of T_1 and T_2 was calculated.

Gaussian 16[16] was used for the (TD)-DFT calculations, CIS(D) and DLPNO-CCSD(T) results were obtained in ORCA 5.0[17], CC2 calculations were performed using Turbomole V7.5[18].

4.2. Thermodynamics of Protonation

Table S1. Stability of julolidine protonated form for molecules **1**-**3** relative to amino group protonation. CAM-B3LYP/def2-TZVPP geometries are used. All values in kJ/mol. Def2-TZVPP was always used.

Level of theory	1	2	3
E(CAM-B3LYP)	-13.9	-10.1	14.7
G(CAM-B3LYP)	-9.9	-8.9	19.1
E(CCSD(T))	-22.0	-15.0	6.0
G(composite[a])	-18.3	-14.0	10.5

[a] composite level of theory, electronic energy difference from CCSD(T) all other thermodynamic terms are calculated at the CAM-B3LYP level.

4.3. Excited State Calculations

Table S2. Vertical excitation energies for all forms of the molecules **1**-**3**. Def2-TZVPP basis set is used, together with SMD solvation model for water solvent. All values in eV.

Form	CAM-B3LYP gas phase	CAM-B3LYP water solvent-SMD	CC2 gas phase
		Molecule **1**	
neutral	3.817	3.550	3.710
-NH_3^+	3.311	3.405	2.878
julolidine protonated	4.178	4.051	4.139
		Molecule **2**	
neutral		3.559	3.719
-NH_3^+		3.423	
julolidine protonated		3.963	3.966
		Molecule **3**	
neutral		3.536	3.628
-NH_3^+		3.404	2.902
julolidine protonated		3.937	3.679
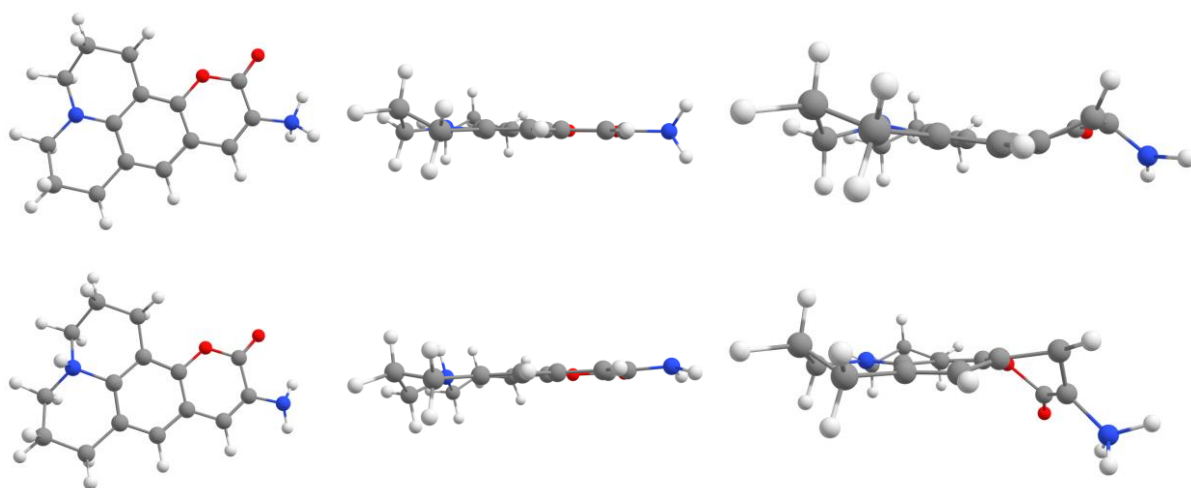
Figure S34. Molecular geometry optimized for the ground state (top view on left side, sideview in the middle column) and geometry near the minimal energy conical intersection MECI (right panel, sideview). First row corresponds to protonation of the NH_2 group, second row protonation of the julolidine moiety.
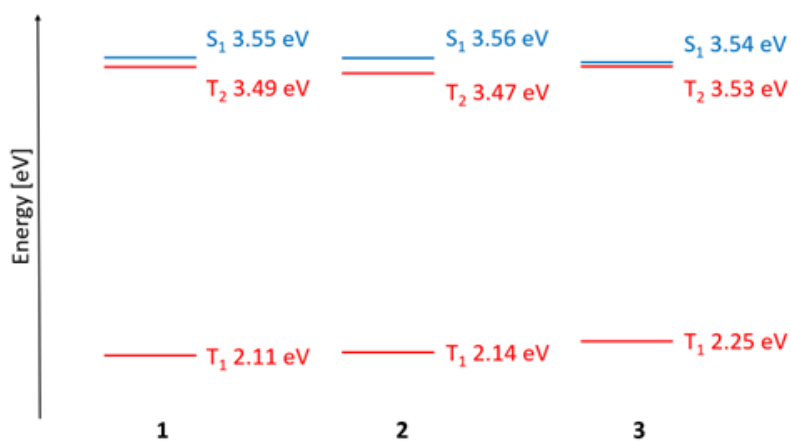
Figure S35. Vertical excitation energy diagram for first triplet (T) and singlet (S) excited states for neutral forms of studied probes **1**-**3**.

Table S3. Nonadiabatic coupling (NAC) elements for vibrational modes of neutral molecule **1**. Freq S_1 are vibrational frequencies of the S_1 state, FCF is Franck-Condon factor for the overlap with vibrational mode in the S_0 state(Freq S_0). Data are arranged in the descending order of NAC. Highlighted are the 3 vibrational modes contributing to the averaged vibrational mode as found in the fitting of experimental fluorescence spectrum (Section 5. Franck-Condon Analysis of Emission Profile).

Freq S_1 [cm^{-1}]	FCF	Freq S_0 [cm^{-1}]	NAC [cm^{-1}]
1664.16	0.74	1653.96	3091.54
1403.89	0.94	1332.27	2265.94
320.62	0.93	304.43	1979.3
1690.22	0.90	1716.21	1473.44
797.1	0.98	813.41	1338.49
44.15	0.85	58.18	1287.67
365.34	0.87	377.45	1250.15
737.32	0.96	747.15	1114.81
474.67	0.96	472.53	1084.84
295.33	0.96	283.56	1058.58
228	0.92	261.2	884.19
267.43	1.00	293.05	748.86
620.92	0.99	632.69	741.2
1393.21	0.99	1393.51	732.71
1559.41	0.91	1707.51	709.4
346.81	0.93	363.04	682.93
1174.48	0.97	1189.29	660.29
133.14	0.67	142.64	639.36
1514.85	1.00	1514.37	613.32
65.82	1.00	69.83	612.07
337.16	0.90	616.64	582.05
398.25	1.00	438.26	576.16
1408.69	1.00	1406.86	572.24
1185.87	0.98	1184.65	556.97
178.89	0.92	189.32	555.15
1370.79	1.00	1381.57	524.4
887.36	1.00	901.37	522.83
769.6	1.00	786.13	501.29
414.62	0.92	417.25	474.04
871.89	1.00	877.49	468.31
419.82	0.97	426.09	466.47
305.79	0.96	325.25	456.67
394.56	0.94	340.33	455.24
459.25	1.00	464.32	444.91
1125.95	0.98	1134.83	428.83
1402.08	0.99	1400.77	418.58
693.82	1.00	714.51	402.25
867.11	1.00	871.42	391.52
1493.17	0.99	1503.37	389.28
1246.08	1.00	1247.83	383.65
1219.51	0.99	1229.29	341.17

1071.59	1.00	1080.23	333.4
170.82	0.93	169.33	331
1482.92	1.00	1489.31	329.41
713.68	0.98	926.41	328.51
1039.49	0.99	1039.93	325.72
1254.73	1.00	1258.75	311
1219.25	1.00	1219.45	303.4
676.61	1.00	683.17	301.42
1382.89	0.99	1383.91	300.68
531.63	1.00	544.58	275.96
1058.81	1.00	1054.8	249.26
1460.1	1.00	1476.7	234
1363.33	0.99	1361.49	231.72
954.86	1.00	959.46	227.9
920.89	1.00	929.87	223.45
553.59	0.99	562.85	202.17
3575.04	0.97	3567.72	199.23
912.81	1.00	955.77	192.34
1306.85	1.00	1305.92	188.48
3222.05	1.00	3196.63	184.84
1313.89	1.00	1313.35	180.49
3013.55	1.00	2983.7	178.21
907.91	1.00	916.08	160.98
100.09	0.97	113.02	152.65
1591.25	1.00	1635.68	145
1486.24	1.00	1487.78	128.02
3010.09	1.00	2984.08	125.12
1106.73	1.00	1108.76	110.38
516.4	0.96	516.75	106.83
982.78	1.00	996.05	103.33
1471.24	0.99	1468.96	100.01
627.98	0.91	646.27	97.28
1229.16	1.00	1240.47	86.64
1270.51	1.00	1268.43	84.28
1111.13	1.00	1117.45	80.62
1395.43	1.00	1438.01	76.28
1610.49	0.99	1603.19	62.38
1568.45	0.99	1550.12	58.57
562.81	1.00	572.94	54.4
3120.52	1.00	3103.79	49.94
3108.64	1.00	3099.61	46.04
3193.36	1.00	3190.97	45.81
3127.24	0.99	3112.84	43.57
3120.14	1.00	3107.53	37.7
84.31	0.96	102.19	32.99
3691.81	0.99	3662.41	31.62
1471.46	1.00	1474.46	30.75
645.95	1.00	815.1	30.41

1048	0.99	1113.21	22.46
3043.16	1.00	3045.14	21.79
3121.67	1.00	3113.85	16.89
3123.45	1.00	3115.75	15.74
1349.4	1.00	1346.41	11.64
1190.62	1.00	1200.44	7.79
1496.33	1.00	1506.73	6.79
3069.19	1.00	3066.15	4.78
3045.27	1.00	3048.46	4.04
3066.96	1.00	3063.15	3.85

Table S4. Nonadiabatic coupling (NAC) elements for vibrational modes of dimethylamine protonated **3**. Freq S_1 are vibrational frequencies of the S_1 state, FCF is Franck-Condon factor for the overlap with vibrational mode in the S_0 state (Freq S_0). Data are arranged in the descending order of NAC. Highlighted is a set of 3 modes with high NAC responsible creating second averaged deactivation mode.

Freq S_1 [cm^{-1}]	FCF	Freq S_0 [cm^{-1}]	NAC [cm^{-1}]
1252.50	0.98	1305.10	2740.57
1184.02	0.97	1185.80	2226.06
1164.29	0.99	1196.77	2012.63
136.96	0.96	123.63	1938.77
493.24	0.99	489.09	1728.69
1711.67	0.98	1606.15	1680.97
307.61	1.00	317.18	1662.17
274.59	0.97	298.32	1605.55
1092.41	0.98	1107.02	1430.13
668.43	0.97	667.25	1307.33
201.52	0.99	199.31	1228.00
623.73	0.95	640.98	1184.05
1535.38	0.97	1641.85	1136.30
1380.11	0.99	1208.89	1063.74
187.11	0.99	188.68	1051.29
1559.43	0.99	1569.07	1022.66
337.04	0.97	346.03	891.38
157.62	1.00	171.77	885.99
127.61	0.99	127.57	838.71
800.15	0.99	815.20	796.20
269.95	1.00	282.23	757.80
75.00	1.00	88.74	753.06
881.24	1.00	894.40	682.97
733.68	0.99	808.38	647.56
1314.82	1.00	1319.56	642.07
742.29	0.96	756.10	635.98
1223.53	1.00	1247.67	617.26
1124.57	1.00	1130.48	574.99
1210.65	1.00	1237.74	522.82
459.06	1.00	450.41	517.34
1563.72	0.99	1694.36	499.95
1243.93	1.00	1248.73	498.47
1336.17	1.00	1377.83	493.66
404.00	1.00	437.40	479.83
1062.71	1.00	1075.44	479.18
705.85	1.00	722.01	479.11
1430.63	1.00	1444.95	467.88
388.11	0.98	394.61	466.88
775.73	0.99	791.98	449.68
1344.49	1.00	1352.92	445.92
1269.70	1.00	1277.83	445.42
1667.78	0.99	1722.12	433.10

1110.68	1.00	1114.78	427.73
254.22	1.00	263.72	416.62
1480.82	1.00	1510.43	414.90
1365.16	1.00	1372.02	394.91
1355.98	0.99	1384.46	389.48
560.80	1.00	567.41	381.60
871.57	1.00	883.46	376.70
260.60	1.00	270.14	358.51
1220.13	1.00	1223.18	342.28
424.76	0.99	424.46	315.42
53.35	1.00	54.44	309.31
1043.37	1.00	1042.72	308.09
534.45	1.00	544.17	307.58
1389.28	1.00	1391.72	298.33
1052.40	0.99	1055.81	292.24
1490.49	1.00	1494.31	287.91
922.31	1.00	931.65	282.59
1103.91	1.00	1111.59	280.14
3016.12	1.00	3015.20	272.99
457.29	1.00	466.11	257.09
1498.11	1.00	1504.37	249.71
1175.41	0.98	1184.13	242.31
35.23	0.94	38.35	239.78
94.19	1.00	101.93	220.08
574.93	1.00	581.82	215.38
1512.92	0.98	1534.62	197.20
1480.14	1.00	1480.93	187.92
1404.68	1.00	1401.99	173.99
70.34	1.00	76.54	170.61
1302.09	1.00	1310.47	168.47
355.24	1.00	370.18	145.52
1471.57	1.00	1479.12	136.73
893.58	1.00	903.80	127.98
1466.08	1.00	1474.69	126.57
1393.57	1.00	1394.79	119.18
1490.01	1.00	1507.44	112.34
1185.18	1.00	1195.31	94.19
619.04	1.00	633.01	93.93
908.13	1.00	915.91	83.95
1255.31	1.00	1262.45	81.47
1491.84	1.00	1492.90	76.05
3115.45	1.00	3107.85	60.88
3204.62	1.00	3200.40	51.47
3130.95	1.00	3120.56	48.00
3128.48	1.00	3113.75	45.90
3105.08	1.00	3105.25	44.34
524.19	0.99	524.65	44.12
3130.20	1.00	3113.05	44.03

979.87	1.00	990.38	43.49
1486.71	1.00	1487.90	41.11
1456.67	1.00	1460.82	39.50
3246.79	1.00	3213.61	38.71
494.96	1.00	503.81	36.38
951.27	1.00	958.95	32.87
3128.24	1.00	3119.36	26.75
1462.60	1.00	1475.79	26.69
653.52	0.99	1006.08	25.98
1476.06	1.00	1485.24	25.06
3012.87	1.00	3014.81	23.88
214.37	1.00	220.76	23.81
3208.32	1.00	3207.34	22.29
3206.91	1.00	3206.32	20.34
3200.41	1.00	3201.84	19.68
914.93	1.00	943.73	18.59
3043.57	1.00	3046.84	17.76
3397.22	1.00	3398.32	17.74
1423.94	1.00	1425.23	14.75
3196.77	1.00	3198.36	8.87
1013.69	1.00	1026.08	8.69
863.59	1.00	875.14	8.51
1063.56	1.00	1065.17	6.86
3071.47	1.00	3065.73	5.39
1484.74	1.00	1487.97	4.68
3102.39	1.00	3102.49	4.49
1402.71	1.00	1413.02	4.18
3074.05	1.00	3068.48	2.94
3140.16	1.00	3121.67	2.55
3044.93	1.00	3050.41	1.58

Table S5. Logarithm of the octanol-water partition factor as predicted by Molinspiration[19] Property Calculator.

Molecule	Log P
7-amino-4-chloromethylcoumarin (CMAC)	1.57
1	2.48
2	2.85
3	3.10

4.4. References

[5]   T. Yanai, D. P. Tew, N. C. Handy, *Chem. Phys. Lett.*, 2004, **393**, 51. doi:10.1016/j.cplett.2004.06.011.

[6]   F. Weigend, R. Ahlrichs, *Phys. Chem. Chem. Phys*, 2005, **7**, 3297. doi:10.1039/B508541A.

[7]   A. V. Marenich, C. J. Cramer, D. G. Truhlar, *J. Phys. Chem. B*, 2009, **113**, 6378. doi:10.1021/jp810292n.

[8]   Y. Guo, C. Riplinger, U. Becker, D. G. Liakos, Y. Minenkov, L. Cavallo, F. Neese, *J. Chem. Phys.*, 2018, **148**, 011101. doi:10.1063/1.5011798.

[9]   M. Head-Gordon, R. J. Rico, M. Oumi, T. J. Lee, *Chem. Phys. Lett.*, 1994, **219**, 21. doi:10.1016/0009-2614(94)00070-0.

[10]   C. Hättig, F. Weigend, *J. Chem. Phys.*, 2000, **113**, 5154. doi:10.1063/1.1290013.

[11] W. Domcke, D. R. Yarkony, H. Köppel, *Conical Intersections: Theory, Computation and Experiment*, World Scientific, Singapore, 2011. doi: 10.1142/7803

[12]   N. Minezawa, M. S. Gordon, *J. Phys. Chem. A*, 2009, **113**, 12749. doi:10.1021/jp908032x.

[13]   F. Neese, F. Wennmohs, U. Becker, C. Riplinger, *J. Chem. Phys.*, 2020, **152**, 224108. doi:10.1063/5.0004608.

[14]   B. de Sousa, F. Neese, R. Izsák, *J. Chem. Phys.*, 2018, **148**, 034104. doi:10.1063/1.5010895.

[15]   (a) Y. Niu, W. Li, Q. Peng, H. Geng, Y. Yi, L. Wang, G. Nan, D. Wang, Z. Shuai, *Mol. Phys.*, 2018, **116**, 1078. doi:10.1080/00268976.2017.1402966.

        (b) Q. Peng, Y. Yi, Z. Shuai, J. Shao, *J. Am. Chem. Soc.*, 2007, **129**, 9333. doi:10.1021/ja067946e.

        (c) Y. Niu, Q. Peng, Z. Shuai, *Sci. China Ser. B-Chem.*, 2008, **51**, 1153. doi:10.1007/s11426-008-0130-4.

        (d) Z. Shuai, *Chin. J. Chem.*, 2020, **38**, 1223. doi:10.1002/cjoc.202000226.

[16]   Gaussian 16, Revision A.03, M. J. Frisch, G. W. Trucks, H. B. Schlegel, G. E. Scuseria, M. A. Robb, J. R. Cheeseman, G. Scalmani, V. Barone, G. A. Petersson, H. Nakatsuji, X. Li, M. Caricato, A. V. Marenich, J. Bloino, B. G. Janesko, R. Gomperts, B. Mennucci, H. P. Hratchian, J. V. Ortiz, A. F. Izmaylov, J. L. Sonnenberg, D. Williams-Young, F. Ding, F. Lipparini, F. Egidi, J. Goings, B. Peng, A. Petrone, T. Henderson, D. Ranasinghe, V. G. Zakrzewski, J. Gao, N. Rega, G. Zheng, W. Liang, M. Hada, M. Ehara, K. Toyota, R. Fukuda, J. Hasegawa, M. Ishida, T. Nakajima, Y. Honda, O. Kitao, H. Nakai, T. Vreven, K. Throssell, J. A. Montgomery, Jr., J. E. Peralta, F. Ogliaro, M. J. Bearpark, J. J. Heyd, E. N. Brothers, K. N. Kudin, V. N. Staroverov, T. A. Keith, R. Kobayashi, J. Normand, K. Raghavachari, A. P. Rendell, J. C. Burant, S. S. Iyengar, J. Tomasi, M. Cossi, J. M. Millam, M. Klene, C. Adamo, R. Cammi, J. W. Ochterski, R. L. Martin, K. Morokuma, O. Farkas, J. B. Foresman, and D. J. Fox, Gaussian, Inc., Wallingford CT, 2016.

[17]   F. Neese, Software update: The ORCA program system—Version 5.0, *WIREs*, 2022, **12**, e1606. doi:10.1002/wcms.1606.

[18]   TURBOMOLE V7.5 2020, a development of University of Karlsruhe and Forschungszentrum Karlsruhe GmbH, 1989-2007, TURBOMOLE GmbH, since 2007; available from http://www.turbomole.com.

[19]   Molinspiration Cheminformatics free web services, https://www.molinspiration.com, Slovensky Grob, Slovakia.

5. Franck-Condon Analysis of Emission Profile

5.1. Emission Spectral Fitting

Emission spectral profiles of the compounds in the low and high pH range were subjected to Franck-Condon analysis using a procedure described in detail elsewhere.[20] In the analysis, the experimental data were fit with an expression shown in Eq. (3):

$$\frac{I(\bar{v})}{I_0} = \sum_{v}^{5} \left[\left(\frac{E_0 - v\hbar\omega_M}{E_0} \right)^3 \frac{S_M^v}{v!} exp \left[-4 \, ln2 \left(\frac{\bar{v} - E_0 + v\hbar\omega_M}{\Delta\bar{v}_{0,1/2}} \right)^2 \right] \right] \tag{3}$$

In Eq. (3) $I(\bar{v})$ is the emitted intensity in quanta, at energy $\bar{v}$ in cm^{-1} and I_0 is the intensity of the 0-0 transition. The quantity v is the vibrational quantum number for the acceptor mode in the ground state, and $\hbar\omega_M$ is the vibrational spacing for the vibrational mode M. As was shown previously,[20-22] in molecules where the vibrational modes primarily responsible for the relaxation of the excited state are closely spaced in energy, these can be grouped together in a representative "averaged" vibrational mode. In this case the $\hbar\omega_M$ represents the weighted sum of the quantum spacings for the grouped vibrational modes contributing to the averaged mode. The quantity S_M is the electron-vibrational coupling constant (Huang-Rhys factor) for the averaged mode. It is related to the change in the equilibrium nuclear displacement (ΔQ_e) between the excited and ground states and to the $\hbar\omega_M$ as shown in Eqs. (4) and (5). The S_M can be expressed as a sum of the S values for the contributing vibrational modes, as shown in Eq. (6).

$$S_M = \frac{1}{2} \left(\frac{M\omega_M}{\hbar} \right) (\Delta Q_e) \tag{4}$$

$$\hbar\omega_M = \sum_j S_j \hbar\omega_j / \sum_j S_j \tag{5}$$

$$S_M = \sum_j S_j \tag{6}$$

In Eq. (4), M is the effective reduced mass of the vibration. In Eqs. 5-6, the sums are over all coupled vibrations j. The quantity $\Delta\bar{v}_{0,1/2}$ in Eq. (3) is the full width at half-maximum of the individual vibronic components in cm^{-1}. It includes contributions from low-frequency, intramolecular vibrations treated classically and the reorganizational energy of the solvent. The quantity E_0 is the $v^*=0 \rightarrow v=0$ energy difference between the excited and ground states in the single-mode approximation.

The comparison of the experimental emission profiles and the best fits of Eq. (3) to the data for the compounds **1-3** are summarized in Figure S36 (neutral pH panels a, c, and e and acidic pH panels b, d and f, respectively). Overall, the analysis yields good quality fits with residuals limited to values below ±5%. The only exception is compound **3** at neutral pH (panel e), where the residuals show large variations due to the very low
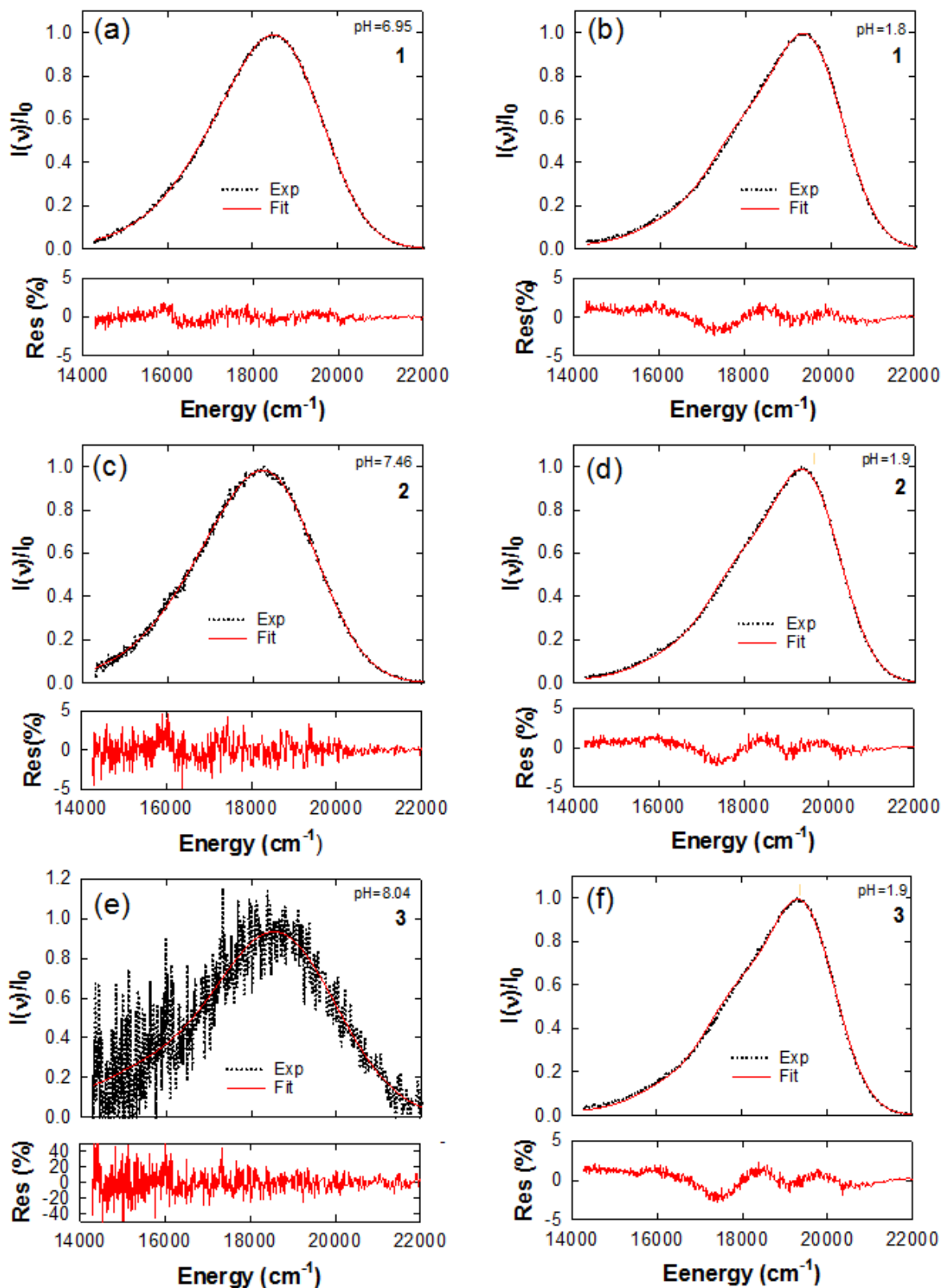
Figure S36. Results of a single-mode approximation Franck-Condon analysis of the emission spectral profiles for compounds **1-3** in neutral pH (panels a, c, e, respectively) and acidic pH (panels b, d, f, respectively). Also shown are the residuals for the difference in between the experimental data and the best fits.

signal levels caused by the low quantum yield of the compound in this pH range. Yet the residuals are symmetrically distributed around the zero value. As described by Eq. (3), the fitting model has four adjustable parameters, E_0, S_M, $\hbar\omega$ and $\Delta v_{0,1/2}$. The values of the adjustable parameters obtained from the fit to the experimental data are summarized in Table S6. The results suggest that the relaxation of the excited states for all three compounds is likely dominated by a group of vibrational modes effectively represented by a single averaged mode with $\hbar\omega$~1500-1600 cm^{-1}. The corresponding E_0 values are in the range ~18,500-18,800 cm^{-1} for the neutral pH and in the range ~19,500 cm^{-1} for acidic pH. The extracted S_M values are in the ~0.53-0.65 range (with the exception of the compound **3** at neutral pH).

Table S6. Summary of the single-mode Franck-Condon analysis of the emission spectral profiles.

Compound	E_0 [cm^{-1}]	S_M	$\hbar\omega_M$ [cm^{-1}]	$\Delta v_{0,1/2}$ [cm^{-1}]
1 pH=6.95	18745±10	0.54±0.01	1509±14	2354±10
1 pH=1.80	19504±4	0.64±0.01	1622±7	1924±6
2 pH=7.46	18558±33	0.61±0.04	1486±43	2540±31
2 pH=1.90	19485±3	0.65±0.01	1594±6	1859±6
3 pH=8.04*	18717±183	0.36±0.17	2176±544	3117±236
3 pH=1.90	19441±4	0.66±0.01	1596±6	1817±7

*The larger error of this set of data is a result of a low signal-to-noise ratio in the measured emission.

The conclusion that the excited state relaxation is likely dominated by a group of vibrational modes ~1500-1600 cm^{-1} is consistent with some earlier analyses of emission profiles of related organic aromatic compounds.[23] However, upon closer inspection of the quality of the spectral fits we noted that the single-mode analyses of profiles at acidic pH (red traces in panels b, d, f) show systematic deviations from the experimental profiles in the range ~16,000 to 20,000 cm^{-1} (see the residual plots in Fig. S36). To further explore the possible origins of this effect, we subjected the emission profiles to analysis by a two-mode Franck-Condon analysis. In this approximation it was assumed there is not a single, but rather two groups of high-frequency (>1000 cm^{-1}) modes responsible for the relaxation of the excited state, which can be represented by two "averaged" modes M_1 and M_2. In this case the fitting model of Eq. (3) is modified to have adjustable parameters, $E_{0,1}$, $E_{0,2}$, $S_{M,1}$, $S_{M,2}$, $\hbar\omega_1$, $\hbar\omega_2$, and $\Delta v_{0,1/2}$. The results of the analysis using the two-mode approximation are shown in Fig. S37 (blue traces). There is an observable, statistically significant improvement in the quality of the fits to the emission profiles of all the compounds in acidic pH. When the two-mode model was applied to the spectra recorded at high pH, we observed no significant improvement in the quality of the fits. The parameters extracted from the two-mode analysis of the low pH emission profiles are summarized in Table S7 (together with the results of the single-mode analysis for data at high pH, same data as in Table S6). The extracted value of the first of the identified vibrational modes, $\hbar\omega_1$~1500 cm^{-1}, is very similar to the one obtained from the one-mode analysis of the
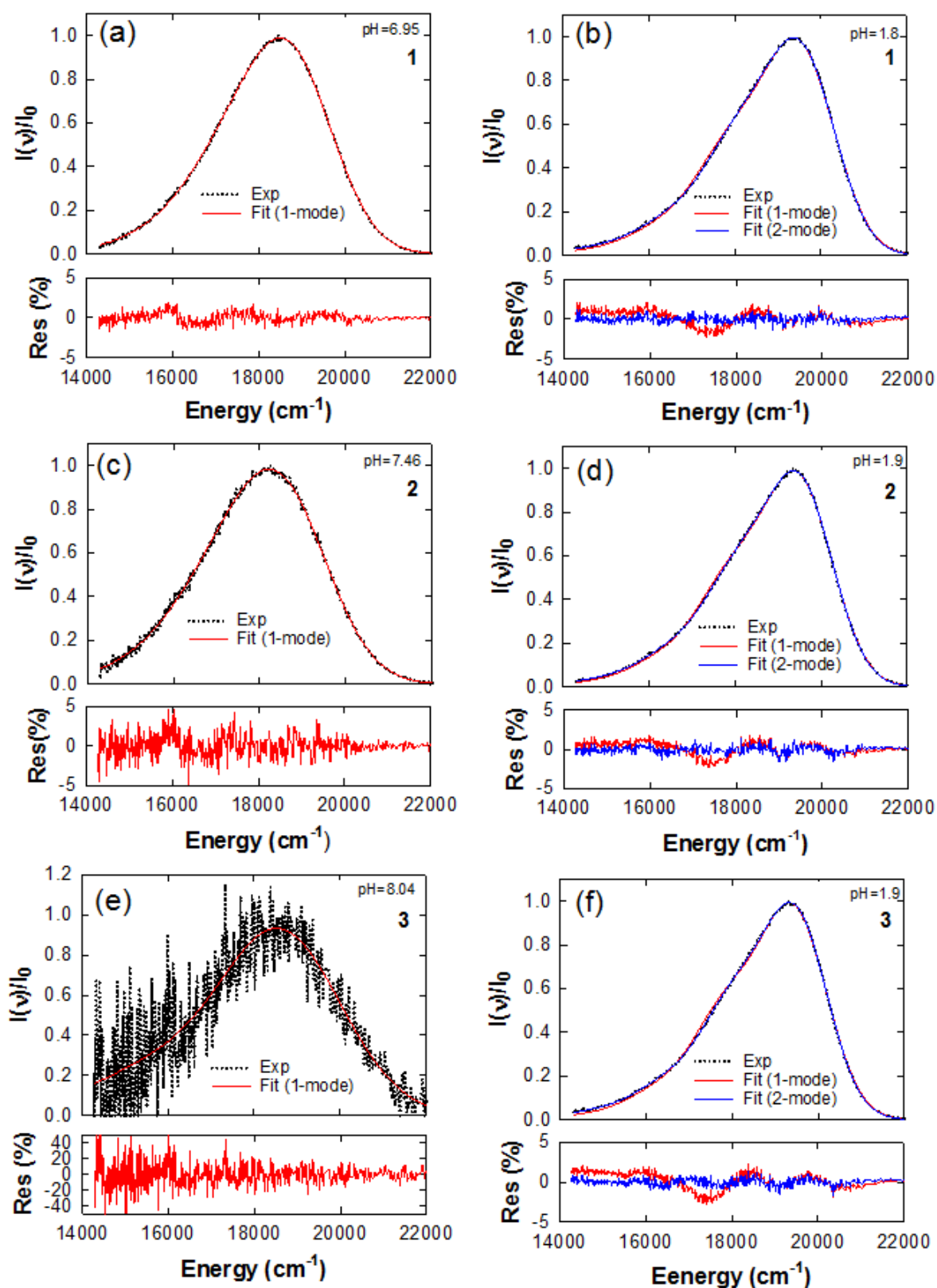
Figure S37. Results of a single and two-mode Franck-Condon analysis of the emission spectral profiles for compounds **1-3** in neutral pH (panels a, c, e, respectively) and acidic pH (panels b, d, f, respectively). Also shown are the residuals for the difference in between the experimental data and the best fits to the single and two-mode models.

profiles at neutral pH. However, the energies associated with the second mode, $\hbar\omega_2$, are distinctly different, with the extracted values ranging between ~1100-1400 cm^{-1}. The values of the Huang-Rhys factors for each of the modes are distinctly different, with $S_{M,1}$ and $S_{M,2}$ being in the range ~0.97-1.04 and ~0.33-0.36, respectively. The values of the $E_{0,1}$, $E_{0,2}$, are very similar for the two modes (~19,500 cm^{-1}), differing by less than ~200 cm^{-1}. The analysis thus suggests that there are possibly two groups of modes with similar E_0 values, but distinctly different $\hbar\omega$ and S_M values that may be contributing to the relaxation of the exited states in the protonated compounds (acidic pH).

Table S7. Summary of the parameters obtained by a one and two-mode Franck-Condon analysis of the emission profiles of compounds **1-3** at low and high pH.

Compound	E_{01} [cm^{-1}]	E_{02} [cm^{-1}]	$S_{M,1}$	$S_{M,2}$	$\hbar\omega_1$ [cm^{-1}]	$\hbar\omega_2$ [cm^{-1}]	$\Delta v_{0,1/2}$ [cm^{-1}]
1 pH=6.95	18745±10		0.54±0.01		1509±14		2354±10
1 pH=1.80	19504±45	19601±63	1.00±0.02	0.33±0.01	1536±28	1253±102	1861±15
2 pH=7.46	18558±33		0.61±0.04		1486±43		2540±31
2 pH=1.90	19526±28	19506±65	0.97±0.01	0.35±0.01	1525±28	1418±62	1815±4
3 pH=8.04[*]	18717±183		0.36±0.17		2176±544		3117±236
3 pH=1.90	19410±38	19572±64	1.04±0.02	0.34±0.02	1505±29	1133±127	1743±22

[*]This set of data has a high noise level due to the weak emission quantum yield of the compounds under the experimental conditions.

The improved quality of the fits with the two-mode approximation, compared to the single mode approximation is, of course, expected given the increased number of adjustable parameters (from four to seven). However, we note that results of the two-mode Franck-Condon analysis described here are in a good agreement with our independent quantum-chemical analysis of the vibrational modes of the compounds **1-3** in neutral and acidic pH, discussed in Section 4. The DFT analysis shows that at neutral pH the strong coupling between the excited and ground state can be primarily attributed to a group of vibrational modes with the frequencies in the range ~1300-1700 cm^{-1} (see Table S3). In contrast, at the low pH there are two groups of mid-frequency vibrational modes, one in ~1300-1700 cm^{-1} range and another in 1000-1200 cm^{-1} range, showing strong coupling between the excited and ground state. Based on this analysis, we conclude that, while at neutral pH the excited state relaxation likely involves only one group of vibrational modes with the frequencies ~1500 cm^{-1}, at low pH there are likely two groups of high frequency vibrational modes contributing to the excited state relaxation; one at ~1500 cm^{-1} and second in the range ~1000-1200 cm^{-1}. The involvement of an additional set of vibrational modes at low pH can be attributed to electronic distortions induced by protonation of the amine groups (see the main text).

5.2. References

[20]   J. V. Caspar, T. J. Meyer, *Inorg. Chem.* 1983, **22**, 2444. doi:10.1021/ic00159a021.

[21]   J. V. Caspar, T. J. Meyer, *J. Am. Chem. Soc.* 1983, **105**, 5583. doi:10.1021/ja00355a009.

[22]   E. M. Kober, J. V. Caspar, R. S. Lumpkin, T. J. Meyer, *J. Phys. Chem.* 1986, **90**, 3722. doi:10.1021/j100407a046.

[23]   M. A. Saidani, A. Benfredj, Z. Ben Hamed, S. Romdhanea, C. Ulbricht, D. A. M. Egbe, H. Bouchriha, *Synth. Metals* 2013, **184**, 83. doi:10.1016/j.synthmet.2013.09.030.

6. Cell imaging

6.1. *E. Coli* Cell Culture and Imaging

E. coli cells were incubated at 37 C in 2xTY culture medium (tryptone 16 g/L, yeast extract 10 g/L, and NaCl 5 g/L) overnight. Then the culture was centrifuged at 10000 rpm for 2 min to collect *E. coli* cells. The sediment was washed with sterile water and then resuspended in culture media with pH (2.00, 4.00, 6.00, 8.00) respectively. Five minutes after resuspension, probe **3** was added into every tube to make the final probe concentration of 4.0 µM. *E. coli* cells were incubated in proper media for 2 h at 37°C, washed in sterile water and then smeared on slides treated with poly-L-lysin and observed with fluorescent microscope Zeiss Axio Imager 2 equipped with Filter Set 38 HE.

6.2. pH Bioimaging in *E. Coli* Cells

The behavior of probe **3** was measured after *in vitro* cultivation of bacteria *E. coli* in media with different pH conditions (pH 2.00, 4.00, 6.00 and 8.00) using Zeiss Axio Imager2 fluorescent microscope. The fluorescence was measured for each condition for 500 ms. The *E. coli* cells displayed strong green fluorescence at low pH 2 (Fig. 6 A-C in the main text) and 4 (Fig. 6 D-F in the main text). The fluorescence signal decreased with increased pH 6 (Fig. 6 G-I in the main text) and 8 (Fig. 6 J-L in the main text).

6.3. Yeast Strains and Growth Conditions

The yeast *Saccharomyces cerevisiae* strain BY4741 (MATa his3Δ1 leu2Δ0 met15Δ0 ura3Δ0)[24] was used in this work. Yeasts cells were grown in 5 mL YPG medium (1% yeast extract, 2% peptone, 3% glycerol) overnight. Next day 50 µL of cell culture was transferred to 5 mL of fresh YPG medium and cultivated till mid-log phase. For vacuolar membrane staining, 500 µL of yeast culture in medium was incubated with 10 µM FM4–64, shaking at 30°C for 60 min. Later, cells were concentrated by centrifugation at 200 g, washed with PBS and incubated with 100 µL of 1 µM coumarin probe **1**, **2**, **3** diluted in water. Immediately, 5 µL of labelled cells were spread on a microscopic slide and covered with the poly-L-lysin coated coverslip and the cells were analyzed immediately. Cells were imaged with an IX83 inverted microscope (Olympus, Tokyo, Japan) equipped with a Planapochromate 60x/1.42 oil objective and CAM-XM10 cooled CCD digital camera. For imaging of compounds **1**, **2** and **3**, U-FCFP filter cube with excitation 425−445 nm and emission 460−510 nm was used. For FM4-64 staining, U-FGWA filter cube with excitation 530-550 nm and emission 575-625 nm was used. For control of the cell morphology, cells were imaged in transmitted light.

6.4. Yeast Vacuolar Staining

pH of yeast vacuolar lumen should vary between 5 and 6 and therefore, based on the relationship between pH and pK_a (Henderson-Hasselbalch equation; Eq. (7)),

$$pH = pK_\mathrm{a} + \log \frac{[\text{conjugate base}]}{[\text{weak acid}]} \tag{7}$$

most of probes **1** (pK_a = 3.43), **2** (pK_a = 3.46) and also **3** (pK_a = 4.23) will be present in solution in their non-protonated forms (even at pH 5). However, fluorescent amines as weak bases can accumulate to very high levels in intracellular organelles acidified by H$^+$-ATPases.[25-27] Particularly quinacrine (atebrin) has been therefore used as generally accepted fluorescent probe for yeast vacuolar staining in the living cells[25]; although the change in quinacrine fluorescence efficiency is rather insignificant in the pH region 5-7 and even slightly increases with increasing pH.[28]

We therefore hypothesize the similar mode of action also for studied weak bases **1** and **2**. Because neutral forms of probes **1** and **2** are sufficiently fluorescent, their accumulation in yeast vacuole offers brighter signal compared to probe **3** with significantly higher pK_a value but low fluorescent quantum yield of its neutral form (Fig. 6 in the main text). In the case of probe **3**, the protonated form contributes dominantly to overall fluorescence response in yeast vacuole even at pH = 5.5 (based on the fluorophore brightness and the corresponding amount of protonated form (~5%), the fluorescent signal of protonated form is approximately twice as high as that of the neutral form). This behaviour supports the previously outlined hypothesis; however, to get deeper insights into the mode of action, further investigation is needed.

6.5. Cytotoxicity of Studied Probes **1**-**3**

Yeast (BY4741) were cultivated in 5 mL of YPD overnight at 28°C. Suspension was diluted in 20 mL of fresh YPD to OD 0.2 and cultivated up to OD 0.5. 1mL of cell suspension was incubated with each fluorescent dye for one hour. Cells were washed in water and the number of cells was calculated. 1000 cells were plated on YPD plates. After 48 hours number of colonies (viable cells) were calculated.
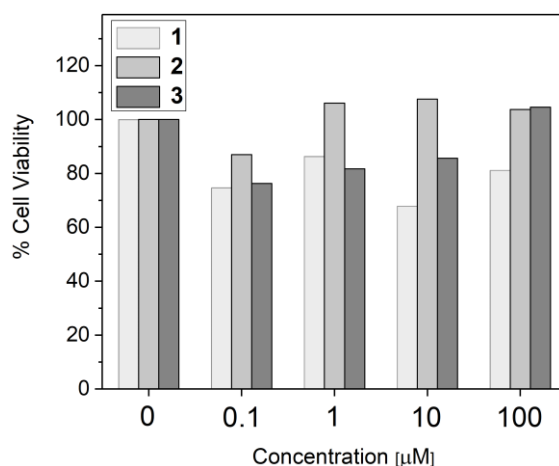

Figure S38. Dependence of yeast cell viability (BY4741) on concentration of studied coumarin probes **1**-**3**.

6.6. References

[24]   C.B. Brachmann, A. Davies, G.J. Cost, E. Caputo, J. Li, P. Hieter, J.D. Boeke, *Yeast* 1998, **14**, 115–132. doi: 10.1002/(SICI)1097-0061(19980130)14:2<115::AID-YEA204>3.0.CO;2-2.

[25] R. A. Preston, R. F. Murphy, E. W. Jones, *Proc. Natl. Acad. Sci. USA*, 1989, **86**, 7027-7031. doi:10.1073/pnas.86.18.7027.

[26] M. Weiss, U. Pick, *Planta*, 1991, **185**, 494-501. doi:10.1007/BF00202958.

[27] N. Hasuzawa, S. Moriyama, L. Wang, A, Nagayama, K. Ashida, Y. Moriyama, M. Nomura, *Purinergic Signalling*, 2021, **17**, 725-735. doi:10.1007/s11302-021-09820-8.

[28] N.-Q. Shi, X.-R. Qi, B. Xiang. *Preparation and Characterization of Drug Liposomes by pH-Gradient Method*. In: W. L. Lu, X. R. Qi, editors. Liposome-Based Drug Delivery Systems. Biomaterial Engineering, Springer, Berlin, Heidelberg; 2018. doi:10.1007/978-3-662-49231-4_18-1.

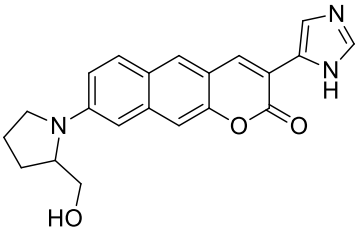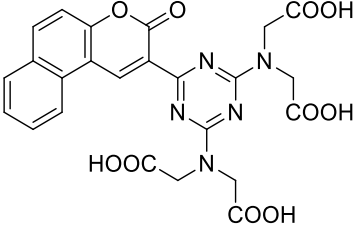# 7. Comparison with other probes
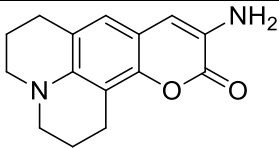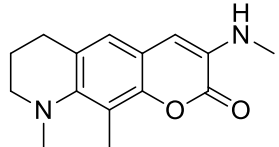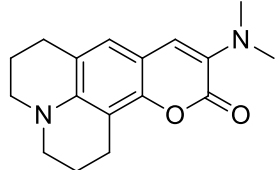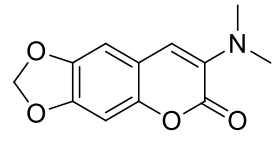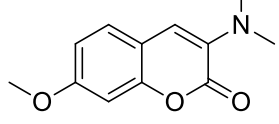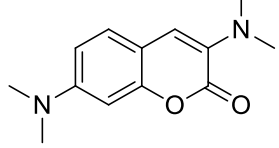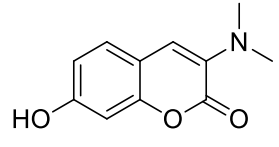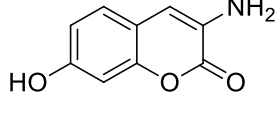
7.1. Design of Studied Probes
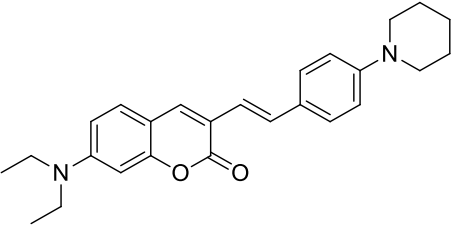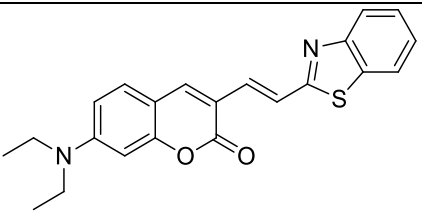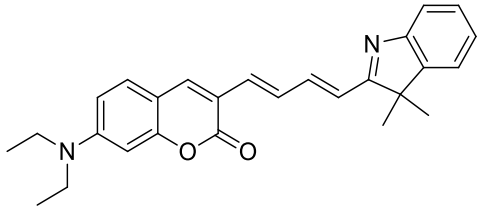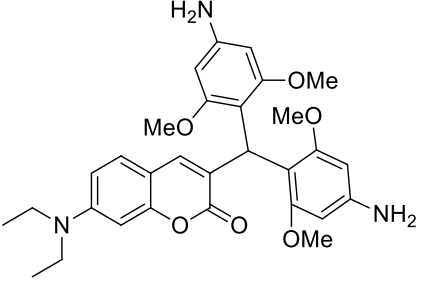
3-aminocoumarin (3-AC) is non-fluorescent over a wide range of pH and its neutral as well as amino-protonated form (with pK_a ~ 1) exhibit fluorescent quantum yields below 5%, similar to the parent coumarin molecule.[29] As generally known, although coumarin itself has a poor quantum yield, an appropriate skeleton substitution leads to fluorescent compounds emitting in the blue–green region. Particularly 7-amino-/7-dialkylamino-coumarins with significant photoinduced intramolecular charge transfer (ICT) belong to to one of the most widespread groups of fluorescent probes.[30] However, their emission efficiency significantly decreases in highly polar solvents due to a presence of nonradiative relaxation pathway associated with formation of twisted intramolecular charge transfer (TICT) state. To eliminate the effect of TICT state formation in highly polar environment, julolidine-fused analogues (for example C153, C102) with rigidized amino group were developed. Unfortunately, reduction of ICT character due to the amino nitrogen atom protonation results in significant drop of their fluorescence efficiency in acidic aqueous solution[31] and these derivatives therefore cannot be used as turn-on pH probes for highly acidic environment. To prepare small molecule fluorescent turn-on pH probes for strongly acidic conditions, it is thus necessary to preserve the ICT character of julolidine-fused coumarins. Therefore, we designed studied 3-aminocoumarins **1**-**3** investigated in this paper and took advantage of the combination of rigidized julolidine skeleton and low pK_a value of the amino group in the position 3 of the parent coumarin.
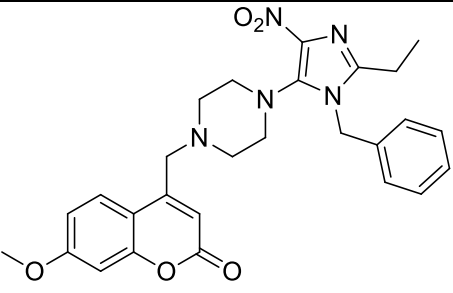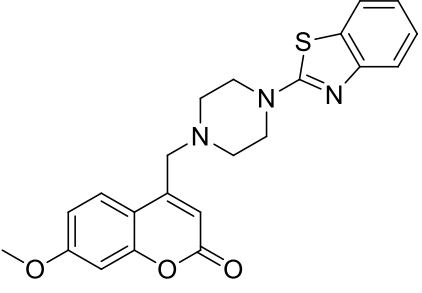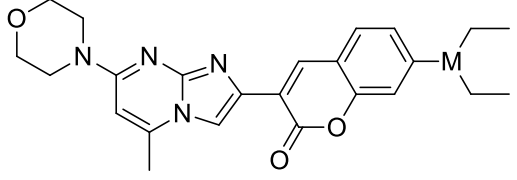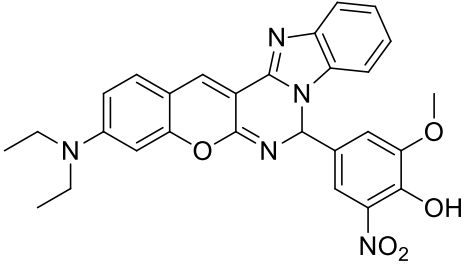
The comparison with commercially used 7-amino-4-chloromethylcoumarin based fluorescent probes for yeast vacuolar lumen staining is described directly in the main text of this publication.

As we described in the main text "While ratiometric approach is a powerful sensing tool, in cases where the probe has a broad emission window, it is difficult to effectively combine multiple probes in a single experiment". Narrow emission profile thus allows multi-color imaging of living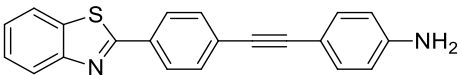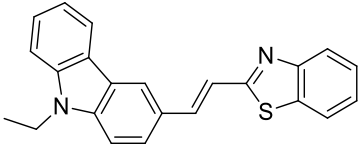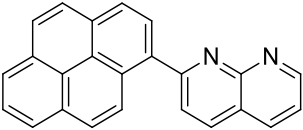 cells, similar to the compared CellTracker™ Blue CMAC Dye (https://www.thermofisher.com/order/catalog/product/C2110; accessed December 2022).
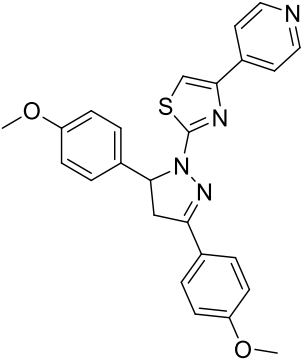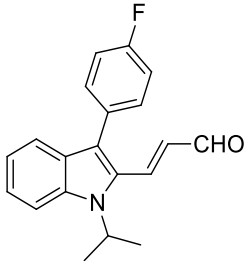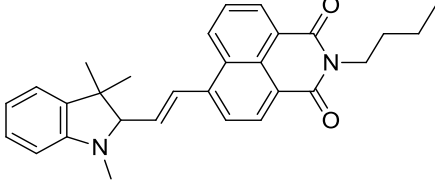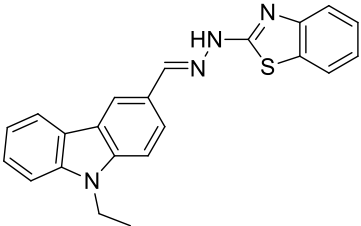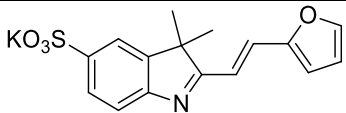
7.2. Comparison with Other Fluorescent pH Probes for Strongly Acidic Conditions from the Literature

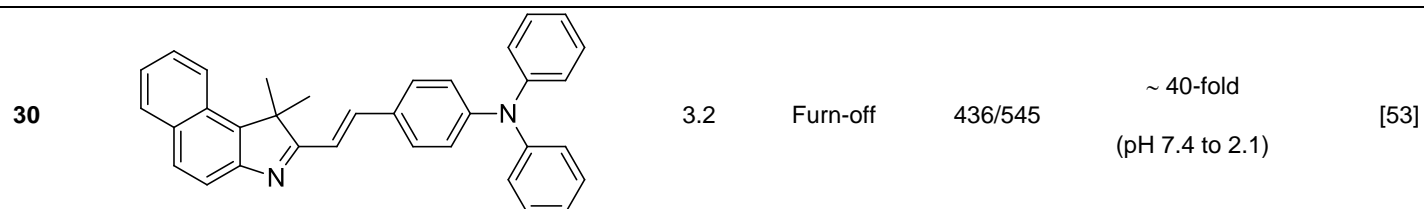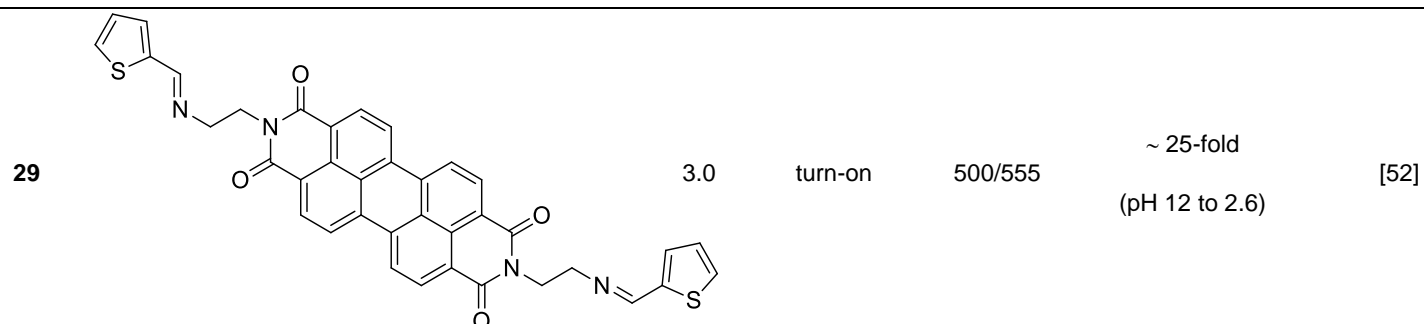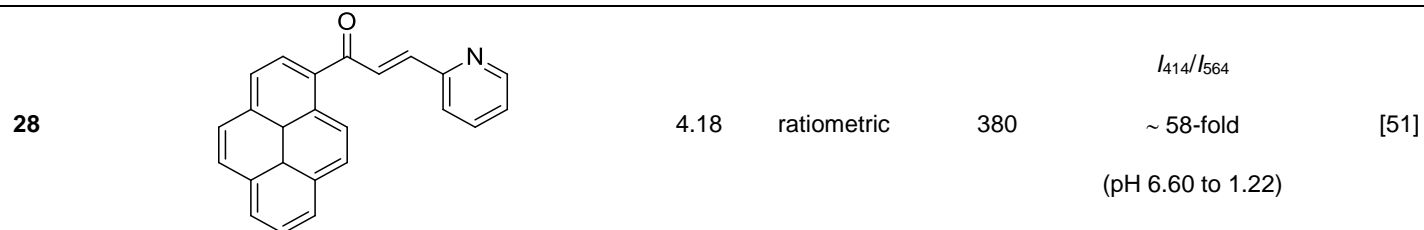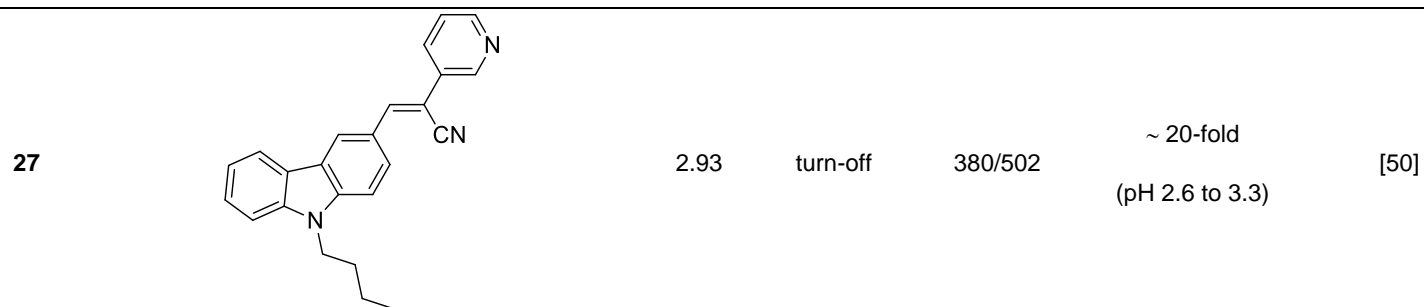| Entry	Probe	pK_a	Type of probe	$\lambda_{ex}/\lambda_{em}$*	Intensity of fluorescence/pH	Reference
1		3.43	turn-on	426/512	~ 2.5-fold (pH 7.67 to 1.81)	this work
2		3.46	turn-on	431/512	~ 9-fold (pH 7.67 to 1.81)	this work
3		4.23	turn-on	435/512	~ 12-fold (pH 7.67 to 1.81)	this work
4		2.9	turn-on	361/450	~ 200-fold (pH 7.67 to 1.81)	our previous work [32]
5		3.0	turn-on	334/406	~ 1340 fold (pH 7.6. to 1.8)	our previous work [32]
6		4.3	turn-on	406/526	~ 12-fold (pH 7.67 to 1.9)	our previous work [32]
7		3.2	turn-on	334/465	~ 1400-fold (pH 7.6 to 1.8)	our previous work [32]
8		2.1	turn-on	332/465	~ 60-fold (pH 5.75 to 1.71)	our previous work [32]

Entry	Probe	pK_a	Type of probe	$\lambda_{ex}/\lambda_{em}$*	Intensity of fluorescence/pH	Reference
			Coumarin Skeleton			
9		4.55	turn-on	400/515	~ 47-fold (pH 5.9 to 3)	[33]
10		2.02	ratiometric	350	I_{536}/I_{410} ~ 18-fold (pH 2 to 7)	[34]
11		3.93	ratiometric	540	I_{722}/I_{600} ~ 16-fold (pH 2 to 7)	[34]
12		2.1	turn-off	385/460	~ 27-fold (pH 0.65 to 3.98)	[35]
13		1.3	ratiometric	375	I_{620}/I_{475} ~ 45-fold (pH 4 to 0.5)	[36]
14		-	ratiometric	373	$I_{400\text{-}470}/I_{471\text{-}600}$ ~ 2.5-fold (pH 1.53 to 6.96)	[37]

Entry	Probe	pK_a	Type of probe	$\lambda_{ex}/\lambda_{em}$*	Intensity of fluorescence/pH	Reference
15	O₂N, N, ethyl, N, benzyl, piperazine, methoxycoumarin structure	4.70	turn-on	321/415	~ 3-fold (pH 8 to 2)	[38]
16	benzothiazole, S, N, piperazine, methoxycoumarin structure; *CB7-encapsulated	3.5	turn-on	$\lambda_{em} = 410$	~ 45-fold (pH 10 to 1)	[39]
17	morpholine, N, imidazopyrimidine, coumarin, M diethyl structure	6.34	turn-on	432/525	~ 15-fold (pH 7 to 3)	[40]
18	diethylamino, O, N, benzimidazole, methoxy, OH, NO₂ structure	2.87	turn-on	505/540	~ 25-fold (pH 2 to 12)	[41]
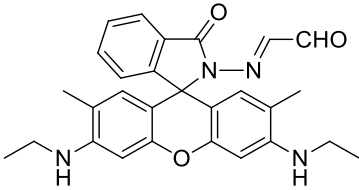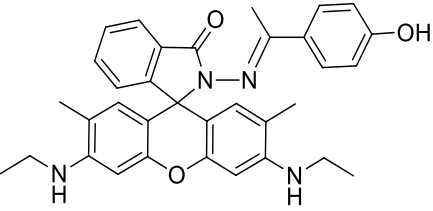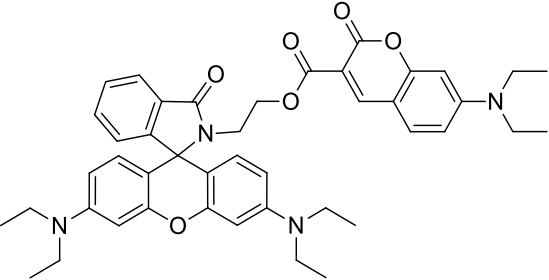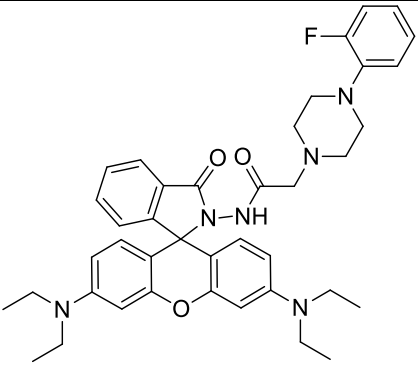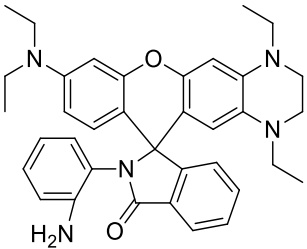
Skeleton with nitrogen heterocycle

19		1.34	turn-off	340/390	~ 300-fold (pH 4.35 to 0.3)	[42]
20		1.62	ratiometric	420	I_{583}/I_{496} ~ 18-fold (pH 3.30 to 1.00)	[43]
21		2.98	turn-off	370/515	~ 20-fold (pH 1.62 to 6.71)	[44]
22		3.52	turn-off	350/460	~ 17-fold (pH 2 to 7)	[45]
23		3.9	ratiometric	365	I_{528}/I_{478} ~ 8-fold (pH 3.5 to 7)	[46]
24		1.6	turn-off	390/430	~ 29-fold (pH 3 to 1)	[47]
25		2.73	turn-off	340/424	~ 1.5-fold (pH 7.4 to 1.64)	[48]
26		4.52	ratiometric	395	I_{514}/I_{571} ~ 7-fold	[49]
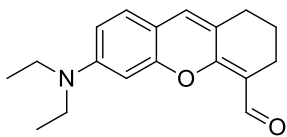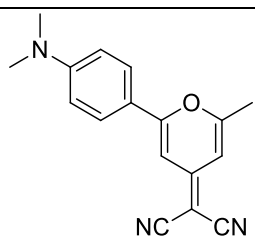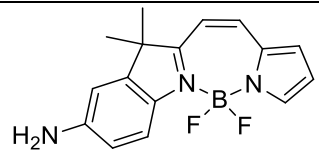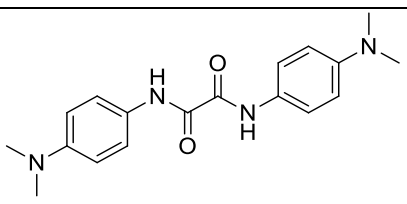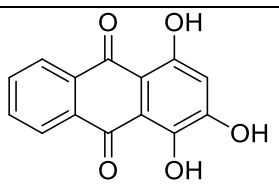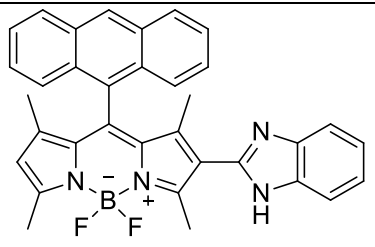
27		2.93	turn-off	380/502	~ 20-fold (pH 2.6 to 3.3)	[50]
28		4.18	ratiometric	380	I_{414}/I_{564} ~ 58-fold (pH 6.60 to 1.22)	[51]
29		3.0	turn-on	500/555	~ 25-fold (pH 12 to 2.6)	[52]
30		3.2	Furn-off	436/545	~ 40-fold (pH 7.4 to 2.1)	[53]

		Rhodamine skeleton				

31		2.32	turn-on	510/560	~ 581-fold (pH 7.5 to 1.1)	[54]
32		2.34	turn-on	510/559	~ 217-fold (pH 5.1 to 1.1)	[55]
33		3.21	ratiometric	420	I_{583}/I_{470} ~ 20-fold (pH 7 to 2)	[56]
34		3.4	turn-on	562/575	~ 11-fold (pH 11 to pH 1.70)	[57]
35		4.83 2.99	ratiometric	530	I_{684}/I_{584} ~ 77-fold (pH 9 to 4) ~ 81-fold (pH 4 to 2)	[58]

Other skeleton

					I_{512}/I_{580}	
36		3.11	ratiometric	400	~ 4-fold (pH 7 to 2.5)	[59]
37		1.17	turn-off	465/540	~ 30-fold (pH 2 to -1)	[60]
38		3.63	turn-on	478/520	(pH 5.01 to 2.47)	[61]
39		-	ratiometric	480	I_{538}/I_{586} ~ 1.5-fold (pH 5 to 1.8)	[62]
40		4.6	turn-on	510/545	~ 7.5-fold (pH 2 to 9)	[63]
41		3.1	turn-on	480/525	pH 1.7 to 8.7	[64]

* for ratiometric probes λ_{ex}

7.3. Structure of CMAC Derivatives
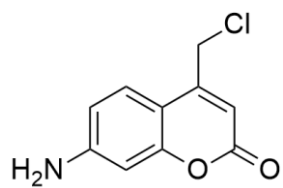
CellTracker™ Blue CMAC
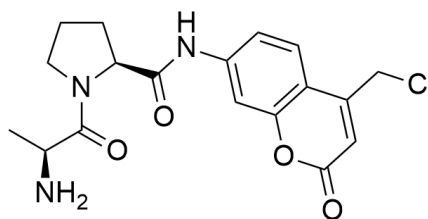
CMAC-Ala-Pro

7.4. References

[29] R. V. S. Rao, M. Krishnamurthy, S. K. Dogra, *J. Photochem.*, 1986, **34**, 55-61. doi:10.1016/0047-2670(86)87051-4.

[30] B. Valeur, M. N. Berberan-Santos, *Molecular Fluorescence: Principles and Applications*, Wiley, Weinheim, 2012.

[31] D. Hessz, B. Hégely, M. Kállay, T. Vidóczy, M. Kubinyi, *J. Phys. Chem. A*, 2014, **118**, 5238-5247. doi:10.1021/jp504496k.

[32] J. Joniak, H. Stankovičová, J. Filo, K. Gaplovská-Kyselá, V. Garaj, M. Cigáň, *Sens. Actuators, B*, 2020, 307, 127646-127655. doi:10.1016/j.snb.2019.127646.

[33] M. Liu, M. Hu, Q. Jiang, Z. Lu, Y. Huang, Y. Tan, Q. Jiang, *RSC Adv.*, 2015, **5**, 15778-15783. doi:10.1039/C4RA11347K.

[34] X.-D. Liu, Y. Xu, R. Sun, Y.-J. Xu, J.-M. Lu, J.-F. Ge, *Analyst*, 2013, **138**, 6542-6550. doi:10.1039/C3AN01033C.

[35] Y. Xu, Z. Jiang, Y. Xiao, F.-Z. Bi, J.-Y. Miao, B.-X. Zhao, *Anal. Chim. Acta*, 2014, **820**, 146-151. doi:10.1016/j.aca.2014.02.029.

[36] H. Kim, S. Sarkar, M. Nandy, K. H. Ahn, *Spectrochim. Acta, Part A*, 2021, **248**, 119088. doi:10.1016/j.saa.2020.119088.

[37] D. Iacopini, A. Moscardini, F. Lessi, V. Di Bussolo, S. Di Pietro, G. Signore, *Bioorg. Chem.*, 2020, **105**, 104372. doi:10.1016/j.bioorg.2020.104372.

[38] N. Saleh, Y. A. Al-Soud, W. M. Nau, *Spectrochim. Acta, Part A.*, 2008, **71**, 818-822. doi:10.1016/j.saa.2008.02.004.

[39] N. Saleh, Y. A. Al-Soud, L. Al-Kaabi, I. Ghosh, W. M. Nau, *Tetrahedron Lett.*, 2011, **52**, 5249-5254. doi:10.1016/j.tetlet.2011.07.138.

[40] B. Aydiner, Z. Seferoglu, *Eur. J. Org. Chem.*, 2018, 5921-5934. doi:10.1002/ejoc.201800594.

[41] A. S. Vasylevska, A. A. Karasyov, S. M. Borisov, C. Krause, *Anal. Bioanal. Chem.*, 2007, **387**, 2134-2141. doi:10.1007/s00216-006-1061-6.

[42] Y. Tan, J. Yu, J. Gao, Y. Cui, Z. Wang, Y. Yang, G. Qian, *RSC Adv.*, 2013, **3**, 4872-4875. doi:10.1039/C3RA00120B.

[43] J. Chao, Y. Liu, J. Sun, L. Fan, Y. Zhang, H, Tong, Z. Li, *Sens. Actuators, B*, 2015, **221**, 427-433. doi:10.1016/j.snb.2015.06.087.

[44] J. Chao, K. Song, Y. Zhang, C. Yin, F. Huo, J. Wang, T. Zhang, *Talanta*, 2018, **189**, 150-156. doi:10.1016/j.talanta.2018.06.073.

[45] X. Zhang, S.-Y. Jing, S.-Y. Huang, X.-W. Zhou, J.-M. Bai, B.-X. Zhao, *Sens. Actuators, B*, 2015, **206**, 663-670. doi:10.1016/j.snb.2014.09.107.

[46] M. Nan, W. Niu, L. Fan, W. Lu, S. Shuang, C. Li, C. Dong, *RSC Adv.*, 2015, **5**, 99739-99744. doi:10.1039/C5RA19180G.

[47] J. Lee, M. H. Lee, *Tetrahedron Lett.*, 2017, **58**, 3178-3182. doi:10.1016/j.tetlet.2017.07.011.

[48] J.-B. Chao, H.-J. Wang, Y.-B. Zhang, Z.-Q. Li, Y.-H. Li, F.-J. Huo, C.-X. Yin, Y.-W. Shi, J.-J. Wang, *Anal. Chim. Acta*, 2017, **975**, 52-60. doi:10.1016/j.aca.2017.04.020.

[49] Y. Zhang, Y. Zhao, B. Song, C. Huang, *Dyes Pigm.*, 2021, **188**, 109205. doi:10.1016/j.dyepig.2021.109205.

[50] J. Chao, H. Wang, K. Song, Z. Li, Y. Zhang, C. Yin, F. Huo, J. Wang, T. Zhang, *Tetrahedron*, 2016, **72**, 8342-8349. doi:10.1016/j.tet.2016.11.013.

[51] J.-B. Chao, Y.-X. Duan, Y.-B. Zhang, C.-X. Yin, M.-G. Zhao, J.-Y. Sun, F.-J. Huo, *Chem. Pap.* 2021, **75**, 3319-3326. doi:10.1007/s11696-021-01572-4.

[52] F. Yie, X.-M. Liang, N. Wu, P. Li, Q. Chai, Y. Fu, *Spectrochim. Acta, Part A*, 2019, **216**, 359-364. doi:10.1016/j.saa.2019.03.049.

[53] Y. Liu, Y. Zhang, J. Wang, A. Yang, Y. Zhao, A. Zhou, R. Xiong, C. Huang, *Bioorg. Chem.*, 2022, **124**, 105792. doi:10.1016/j.bioorg.2022.105792.

[54]   M. Tian, X. Peng, J. Fan, J. Wang, S. Sun, *Dyes Pigm.*, 2012, **95**, 112-115. doi:10.1016/j.dyepig.2012.03.008.

[55]   L. Liu, P. Guo, L. Chai, Q. Shi, B. Xu, J. Yuan, X. Wang, X. Shi, W. Zhang, *Sens. Actuators, B*, 2014, **194**, 498-502. doi:10.1016/j.snb.2013.12.023.

[56]   S.-L. Shen, X.-F. Zhang, S.-Y. Bai, J.-Y. Miao, B.-X. Zhao, *RSC Adv.*, 2015, **5**, 13341-13346. doi:10.1039/C4RA16398B.

[57]   J.-L. Tan, M.-X. Zhang, F. Zhang, T.-T. Yang, Y. Liu, Z.-B. Li, H. Zuo, *Spectrochim. Acta, Part A*, 2015, **140**, 489-494. doi:10.1016/j.saa.2014.12.110.

[58]   J. Gong, C. Liu, X. Jiao, S. He, L. Zhao, X. Zeng, *Spectrochim. Acta, Part A*, 2020, **243**, 118821. doi:10.1016/j.saa.2020.118821.

[59]   Z.-X. Tong, W. Liu, H. Huang, H.-Z. Chen, X.-J. Liu, Y.-Q. Kuang, J.-H. Jiang, *Analyst*, 2017, **142**, 3906-3912. doi:10.1039/C7AN01103B.

[60]   D.-Y. Kim, J. N. Kim, H. J. Kim, *Spectrochim. Acta, Part A*, 2014, **122**, 304-308. doi:10.1016/j.saa.2013.11.035.

[61]   X. Yuan, T. Zhang, J. Yan, X. Chen, L. Wang, X. Liu, K. Zheng, N. Zhang, *Dyes Pigm.*, 2020, **177**, 108318. doi:10.1016/j.dyepig.2020.108318.

[62]   C. Li, H. Ge, D. Zhang, C. Sun, S. Yue, X.-D. Jiang, J. Du, *Sens. Actuators, B*, 2021, **344**, 130-213. doi:10.1016/j.snb.2021.130213.

[63]   S. Mahanty, K. Rathinasamy, D. Suresh, *J. Fluoresc.*, 2022, **32**, 247-256. doi:10.1007/s10895-021-02836-8.

[64]   R. C. R. Goncalves, E. Belmonte-Reche, J. Pina, M. C. da Silva, S. C. S. Pinto, J. Gallo, S. P. G. Costa, M. M. M. Raposo, *Molecules*, 2022, **27**, 8065. doi:10.3390/molecules27228065.